

# A Comparative Study of Knots of Star Formation in Interacting vs. Spiral Galaxies

Beverly J. Smith<sup>1</sup>, Javier Zaragoza-Cardiel<sup>2</sup>, Curtis Struck<sup>3</sup>, Susan Olmsted<sup>1</sup>, Keith Jones<sup>1</sup>

## ABSTRACT

Interacting galaxies are known to have higher global rates of star formation on average than normal galaxies, relative to their stellar masses. Using UV and IR photometry combined with new and published  $H\alpha$  images, we have compared the star formation rates of  $\sim 700$  star forming complexes in 46 nearby interacting galaxy pairs with those of regions in 39 normal spiral galaxies. The interacting galaxies have proportionally more regions with high star formation rates than the spirals. The most extreme regions in the interacting systems lie at the intersections of spiral/tidal structures, where gas is expected to pile up and trigger star formation. Published Hubble Telescope images show unusually large and luminous star clusters in the highest luminosity regions. The star formation rates of the clumps correlate with measures of the dust attenuation, consistent with the idea that regions with more interstellar gas have more star formation. For the clumps with the highest star formation rates, the apparent dust attenuation is consistent with the Calzetti starburst dust attenuation law. This suggests that the high luminosity regions are dominated by a central group of young stars surrounded by a shell of clumpy interstellar gas. In contrast, the lower luminosity clumps are bright in the UV relative to  $H\alpha$ , suggesting either a high differential attenuation between the ionized gas and the stars, or a post-starburst population bright in the UV but faded in  $H\alpha$ . The fraction of the global light of the galaxies in the clumps is higher on average for the interacting galaxies than for the spirals. Thus the star forming regions in interacting galaxies are more luminous, dustier, or younger on average.

*Subject headings:* galaxies: interactions—galaxies: starburst

## 1. Introduction

Since the pioneering study of Larson & Tinsley (1978), numerous studies have concluded that gravitational interactions between galaxies can trigger star formation (Lonsdale, Persson, & Matthews 1984; Keel et al. 1985; Bushouse 1987; Bushouse, Lamb, & Werner 1988; Kennicutt et al. 1987; Barton, Geller, & Kenyon 2000; Barton Gillespie, Geller, & Kenyon 2003; Lambas et al. 2003; Nikolic, Cullen, & Alexander 2004; Woods, Geller, & Barton 2006; Smith et al. 2007; Lin et al. 2007; Ellison et al. 2008; Li et al. 2008; Freedman Woods et al. 2010). Observations in the  $H\alpha$  line (Bushouse 1987; Kennicutt et al. 1987), the far-infrared (Bushouse 1987; Bushouse, Lamb, & Werner 1988; Kennicutt et al. 1987), and the mid-infrared (Lonsdale, Persson, & Matthews 1984; Smith et al. 2007; Lin et al. 2007) along with optical spectroscopic studies (Li et al. 2008) indicate that the global star formation rates (SFRs) of strongly interacting pre-merger galaxy pairs are enhanced by about a factor of 2 – 3 on average relative to their stellar masses compared to normal galaxies, however, there is significant scatter from galaxy to galaxy. On average, closer pairs tend to have higher rates of star formation (Barton, Geller, & Kenyon 2000; Barton Gillespie, Geller, & Kenyon 2003; Lambas et al. 2003; Nikolic, Cullen, & Alexander 2004; Woods, Geller, & Barton 2006; Freedman Woods et al.

<sup>1</sup>Department of Physics and Astronomy, East Tennessee State University, Johnson City TN 37614; Southeastern Association for Research in Astronomy; smithbj@etsu.edu

<sup>2</sup>Instituto de Astrofísica de Canarias, La Laguna, Tenerife, Spain; Now at Instituto de Astronomía, Universidad Nacional Autónoma de México, Mexico City, Mexico

<sup>3</sup>Department of Physics and Astronomy, Iowa State University, Ames IA 50011

2010; Lin et al. 2007; Li et al. 2008). The star formation in interacting galaxies is often centrally-concentrated (Lonsdale, Persson, & Matthews 1984; Keel et al. 1985; Bushouse 1987; Smith et al. 2007), likely due to angular momentum transfer driving gas into the inner core (e.g., Barnes & Hernquist 1991, Mihos & Hernquist 1996, Di Matteo et al. 2007).

In addition to enhanced nuclear star formation, strong star formation is sometimes seen in the outer disks and tidal structures of interacting galaxies (Schweizer 1978; Mirabel, Lutz, & Maza 1991; Mirabel, Dottori, & Lutz 1992; Hibbard & van Gorkom 1996; Smith et al. 2010). The tidal structures of interacting galaxies frequently display star formation morphologies that usually are not seen in isolated galaxies. These include: 1) regularly-spaced star formation regions (‘beads on a string’) along tidal features and spiral arms (Hancock et al. 2007; Smith et al. 2010), 2) massive concentrations of stars and gas near the ends of tidal features, the so-called tidal dwarf galaxies (TDGs) (e.g., Duc & Mirabel 1994; Duc et al. 1997, 2000; Smith et al. 2010), 3) luminous star forming regions at the base of tidal features (‘hinge clumps’, Hancock et al. 2009; Smith et al. 2010, 2014), and 4) gas-rich star-forming structures produced by accretion from one galaxy to another (e.g., Smith et al. 2008). Beads-on-a-string may be indicative of the accumulation scale of local gravitational instabilities (e.g., Elmegreen & Efremov 1996), while TDGs and some accretion star formation may result from gas pile-ups and subsequent gravitational collapse (Duc, Bournaud, & Masset 2004; Wetzstein, Naab, & Burkert 2007; Smith et al. 2008). Hinge clumps may be produced by converging flows of dissipative gas along caustics, where a caustic is a narrow pile-up zone caused by orbit crowding (Struck & Smith 2012; Smith et al. 2014). Hinge clumps, accretion knots, and TDGs, although rare in the local Universe, were likely much more common in the past. Hinge clumps bear an intriguing resemblance to the massive star forming clumps seen in high redshift disks (e.g., Elmegreen et al. 2009; Förster Schreiber et al. 2011), while the prolonged infall out of a tidal tail may be the best local analog to cold accretion onto galaxies, evidently a common process in the early Universe, but not in the present.

Theoretical studies suggest that gas turbulence and pressure are enhanced in galaxy mergers, potentially leading to larger Jeans masses, more massive star forming regions, larger fractions of dense gas, and more efficient star formation (Elmegreen, Kaufman, & Thomasson 1993; Bournaud, Duc, & Emsellem 2008; Teyssier, Chapon, & Bournaud 2010; Bournaud et al. 2011; Renaud, Kraljic, & Bournaud 2012; Powell et al. 2013; Renaud et al. 2014). Consistent with this scenario, larger gas velocity dispersions have been found in some interacting galaxies (Elmegreen, Kaufman, & Thomasson 1993; Irwin 1994; Elmegreen et al. 1995; Zaragoza-Cardiel et al. 2013, 2014, 2015). Based on the observed velocity dispersion measurements, Zaragoza-Cardiel et al. (2013, 2014, 2015) have concluded that the highest mass star forming regions in interacting galaxies are gravitationally-bound, while lower mass regions are pressure-confined. This suggests a different mode of star formation may be operating in the highest luminosity regions.

In spiral galaxies, the global SFR depends upon the gas surface density via a power law relation (Schmidt 1959; Kennicutt 1989, 1998). Within the disks of nearby spirals, a similar relation is found on smaller spatial scales (Kennicutt et al. 2007; Liu et al. 2011). However, extreme starburst galaxies (many of which are interacting or merging) may have enhanced star formation relative to the gas content compared to the relationship for spirals (Daddi et al. 2010; Genzel et al. 2010; Saintonge et al. 2012; Silverman et al. 2015), suggesting the existence of a distinct starburst ‘mode’ of star formation. Such a mode had been predicted earlier on the basis of theoretical arguments, with the starburst phase being limited by stellar feedback (Scalo & Struck-Marcell 1986; Quillen & Bland-Hawthorn 2008). High resolution simulations suggest that increased gas turbulence, cloud filamentation, and cloud fragmentation in interacting galaxies may lead to more efficient star formation (Teyssier, Chapon, & Bournaud 2010; Renaud et al. 2014). However, the existence of two distinct modes of star formation is uncertain (Kennicutt 1998; Powell et al. 2013).

In addition to having higher SFRs, interacting galaxies may have more obscured young stars on average. Interacting galaxies have larger far-infrared-to- $H\alpha$  luminosities on average than isolated systems (Bushouse 1987), suggesting higher

H $\alpha$  extinctions in the interacting systems. The global optical and UV colors of interacting galaxies show a larger dispersion than those of normal systems (Larson & Tinsley 1978; Sol Alonso et al. 2006; Smith & Struck 2010), likely a consequence of both more young stars and more dust attenuation. Global UV-to-MIR ratios also imply larger attenuations in galaxy pairs than in normal galaxies (Yuan et al. 2012). As gas gets driven into the central regions of galaxies by an interaction, not only is the SFR increased but also the dust column density.

More generally, the dust attenuation in galaxies tends to increase with increasing SFR (Wang & Heckman 1996; Buat & Burgarella 1998; Buat et al. 1999; Hopkins et al. 2001; Sullivan et al. 2001). The galaxies with the highest far-infrared luminosities ( $L_{\text{FIR}}$ ) are generally interacting or merging systems (Smith et al. 1987; Armus, Heckman, & Miley 1987; Sanders et al. 1988; Melnick & Mirabel 1990; Leech et al. 1994; Clements & Baker 1996; Clements et al. 1996; Sanders & Mirabel 1996; Rigopoulou et al. 1999). The highest  $L_{\text{FIR}}$  galaxies have large far-infrared-to-optical ratios (Smith et al. 1987; Armus, Heckman, & Miley 1987) implying high dust attenuation.

How much the starlight in a galaxy is attenuated at each wavelength depends upon the amount of dust, the type of dust, and the distribution of the dust relative to the stars. Differences in the assumed geometry of the system can cause large variations in the implied dust attenuation law (Natta & Panagia 1984; Witt & Gordon 2000; Charlot & Fall 2000; Granato et al. 2000; Wild et al. 2011). Contributing factors include the clumpiness of the gas, the fraction of diffuse dust vs. dust associated with the birth cloud, and the relative amounts of attenuation of stars of various ages. There is evidence that the dust attenuation law in normal spirals may differ from that in starbursts (Burgarella, Buat, & Iglesias-Páramo 2005; Panuzzo et al. 2007; Boquien et al. 2009, 2012; Conroy, Schiminovich, & Blanton 2010; Mao, Kong, & Mullan 2014). The assumed corrections for dust attenuation can make large differences in the inferred SFRs, luminosities, and stellar masses of galaxies. At present, there is considerable uncertainty in the attenuation law applicable for different types of galaxies.

To better understand star formation trigger-

ing mechanisms and dust attenuation in interacting galaxies, spatially-resolved studies of nearby galaxies are crucial. By combining multi-wavelength observations of individual star forming regions in the galaxies with numerical simulations of the interaction, we can better identify what is triggering the star formation in that particular system. Over the last several years, we have conducted detailed multi-wavelength studies of star-forming ‘clumps’ within five individual galaxy pairs using aperture diameters of 0.8 – 6.2 kpc, and have constructed matching numerical models of the interactions: Arp 82 (Hancock et al. 2007), Arp 107 (Smith et al. 2005; Lapham, Smith, & Struck 2013), Arp 284 (Struck & Smith 2003; Smith, Struck, & Nowak 2005; Peterson et al. 2009), Arp 285 (Smith et al. 2008), and Arp 305 (Hancock et al. 2009). Other researchers have done similar studies of regions in other interacting galaxies (e.g., Arp 24: Cao & Wu 2007; Arp 85: Calzetti et al. 2005, 2007; Arp 158: Boquien et al. 2011; Arp 244: Zhang, Gao, & Kong 2010; NGC 2207/IC 2163: Elmegreen et al. 1995, 2001, 2006; Struck et al. 2005; Kaufman et al. 2012). These ‘clumps’ are star formation complexes containing multiple star clusters (e.g., Elmegreen et al. 2006; Peterson et al. 2009; Smith et al. 2014).

Such studies of individual systems provide clues to star formation triggering mechanisms on a case-by-case basis, however, they do not give much information about how important statistically the different processes are to galaxy evolution as a whole. For a more comprehensive understanding of star formation and dust attenuation in interacting galaxies, surveys of regions within multiple galaxies would be valuable. A few such comparative studies have been done recently (Boquien et al. 2009, 2010; Lapham, Smith, & Struck 2013; Smith et al. 2014), but they only involve a handful of galaxies.

In the current study, we describe a systematic multi-wavelength investigation of the star forming regions within a sample of 46 interacting galaxy pairs, and compare with a matching set of normal spiral galaxies. This is a much larger number of galaxies than included in earlier such surveys. We have extracted UV/optical/IR photometry for star forming regions within these galaxies, and have estimated SFRs and dust attenuations for these

regions. In Section 2 of this paper, our samples of galaxies are discussed in detail. Our datasets are described in Section 3. For this study, we acquired new narrowband  $H\alpha$  images of some of the systems; these observations are described in Section 3. The clump selection and photometry is discussed in Section 4. The star formation rates for the regions are discussed in Section 5. In Section 6, we discuss the dust attenuation in the clumps. Our results are summarized in Section 7.

## 2. Galaxy Samples

In this study, we compare the properties of star forming regions within interacting galaxies with those in normal spiral galaxies. The selection of these samples is described below.

### 2.1. Pre-Merger Interacting Galaxies with Strong Tails and Bridges

For the interacting galaxies, we use our ‘Spirals, Bridges, and Tails’ (SB&T) sample (Smith et al. 2007, 2010). This consists of more than three dozen pre-merger galaxy pairs chosen from the Arp (1966) Atlas of Peculiar Galaxies to be relatively isolated binary systems with strong tidal distortions; we eliminated merger remnants, close triples, and multiple systems. They have radial velocities  $<10,350 \text{ km s}^{-1}$  and angular sizes  $\geq 3'$ . The interacting pair NGC 4567/8 was included in the SB&T sample in Smith et al. (2007), as it fits this basic selection criteria although it is not in the Arp Atlas. To the original SB&T sample, we have added a few additional Arp systems with slightly smaller angular sizes that were not in our earlier studies. We have also added the similar system NGC 2207/IC 2163 (Elmegreen et al. 1995, 2001, 2006), which is not in the Arp Atlas.

Only galaxies with Spitzer  $8 \mu\text{m}$  maps covering both galaxies in the pair were included in the final sample for the current study, since we use the  $8 \mu\text{m}$  images to select the target star forming regions (see Section 4). Our final sample of interacting galaxies contains 46 pairs<sup>1</sup>. This sample is given in Table 1, along with the distance to each system, the far-infrared luminosity, the total

$H\alpha$  luminosity, and the reference for the  $H\alpha$  luminosity. Throughout this paper we use distances from the NASA Extragalactic Database (NED<sup>2</sup>), assuming  $H_0 = 73 \text{ km s}^{-1} \text{ Mpc}^{-1}$  and accounting for peculiar velocities due to the Virgo Cluster, the Great Attractor, and the Shapley Supercluster. A histogram of the distances to the sample galaxies is provided in the top panel of Figure 1.

The SB&T galaxies are relatively simple systems compared to many interacting galaxies, for example, galaxies in compact groups or more advanced mergers, thus they are more suitable for the detailed matching of simulations to observations. By excluding advanced mergers from our sample, we are omitting some of the most extreme starbursts in the local Universe, which are sometimes later-stage mergers than our sample galaxies (e.g., Melnick & Mirabel 1990; Rigopoulou et al. 1999). The galaxies in our interacting sample contain the closest and best-studied examples of strong tidal tails and bridges in the local Universe, with a median distance of only 48 Mpc. This is much closer than other samples selected from other surveys, for example, the Sloan Digitized Sky Survey (SDSS) selected TDGs studied by Kaviraj et al. (2012) have a median distance of 220 Mpc, while the Torres-Flores et al. (2009) compact groups containing TDGs have a median distance of 62 Mpc. The SB&T sample contains about a dozen examples of ‘beads on a string’ and about half a dozen ‘hinge clumps’. It also contains 11 candidate TDGs, and about half a dozen extended structures likely caused by mass transfer between galaxies (Smith et al. 2010).

### 2.2. A ‘Control’ Sample of Spiral Galaxies

In Smith et al. (2007), we compared the distribution of Spitzer broadband mid-infrared colors for the SB&T galaxies with those of a sample of 26 ‘normal’ spirals selected from the SINGS sample (Kennicutt et al. 2003), after eliminating SINGS galaxies with massive nearby companions (i.e., velocity difference  $\leq 1000 \text{ km s}^{-1}$ , optical luminosity  $> 1/10$  the target galaxy, and separation from the target galaxy of  $< 10$  times the diameter of target galaxy or the companion, whichever is larger). In Smith & Struck (2010), we constructed an alternative control sample of spirals. We started with

<sup>1</sup>Arp 297 consists of two pairs at different redshifts, Arp 297S and Arp 297N. These two pairs are treated separately in this analysis.

<sup>2</sup><http://ned.ipac.caltech.edu>

the ‘GALEX Ultraviolet Atlas of Nearby Galaxies’ (Gil de Paz et al. 2007), and selected the subset with SDSS images that are classified as normal spirals and have distances  $< 143$  Mpc. NED and available GALEX/SDSS images are used to eliminate galaxies with nearby massive companions, leaving a total of 121 spiral galaxies. We compared the large-scale environments and blue luminosity distribution of this sample with those of the SB&T sample, and found they are statistically indistinguishable (Smith & Struck 2010).

In the current study, our final control sample of spirals (Table 2) consists of all 39 of the galaxies in the union of these two spiral samples that have Spitzer  $8\ \mu\text{m}$  images available. A histogram of the distances to the sample spiral galaxies is provided in the bottom panel of Figure 1. The median distance to the spiral galaxies is 14 Mpc, thus the spirals are on average closer than the interacting systems. Later in this paper, we investigate the subset of galaxies closer than 67 Mpc separately (see Section 4.1). All but two of the spirals are within 67 Mpc, while 16 out of the 46 interacting pairs have distances greater than 67 Mpc.

In the top panel of Figure 2, we provide a histogram of the global Spitzer  $3.6\ \mu\text{m}$  luminosities ( $\nu L_\nu$ ) of the individual galaxies in the interacting galaxy pairs. The total  $3.6\ \mu\text{m}$  fluxes were obtained from Spitzer images (Section 3) as in Smith et al. (2007). The lower panel of Figure 2 shows a similar histogram for the spiral galaxies. The global Spitzer  $3.6\ \mu\text{m}$  luminosities  $L_{3.6}$  of galaxies is an approximate measure of their stellar mass, as it is usually dominated by the light from older stars (e.g., Helou et al. 2004). Figure 2 shows that the spirals and the interacting galaxies have similar distributions of  $L_{3.6}$ , thus there are not large differences between the stellar masses of the galaxies in the two samples on average. Proportionally, there are a few more lower luminosity galaxies in the interacting sample, likely because of the inclusion of low mass companion galaxies. The interacting galaxy sample also contains a few more higher luminosity galaxies than the spiral sample. The subset of interacting galaxies with distances less than 67 Mpc has a  $L_{3.6}$  distribution very similar to that of the spiral sample.

### 3. Datasets

In this study, we use GALEX near-UV (NUV) and far-UV (FUV) maps, along with Spitzer near-infrared ( $3.6\ \mu\text{m}$  and  $4.5\ \mu\text{m}$ ) and mid-infrared ( $5.8\ \mu\text{m}$ ,  $8.0\ \mu\text{m}$ , and  $24\ \mu\text{m}$ ) images. We also include new and archived  $\text{H}\alpha$  images in this study. An Atlas of the Spitzer infrared images of the SB&T galaxies was published in Smith et al. (2007). A second Atlas of the SB&T galaxies displaying the GALEX and corresponding SDSS images was published in Smith et al. (2010). The global UV, optical, and IR properties of the SB&T galaxies were compared with those of normal spiral galaxies in Smith et al. (2007, 2010) and Smith & Struck (2010).

The  $3.6\ \mu\text{m} - 8.0\ \mu\text{m}$  images were acquired using the Spitzer Infrared Array Camera (IRAC; Fazio et al. 2004), while the  $24\ \mu\text{m}$  images were obtained with the Spitzer Multiband Imaging Photometer for Spitzer (MIPS; Rieke et al. 2004). The Spitzer images used in the current study were acquired from the Spitzer Heritage Archive<sup>3</sup>, except for four large angular size SINGS galaxies, for which larger mosaicked images were obtained from the NED image database. The  $24\ \mu\text{m}$  images have  $2''.45\ \text{pixel}^{-1}$ . The  $3.6\ \mu\text{m} - 8\ \mu\text{m}$  images from the Heritage archives have  $0''.6\ \text{pixel}^{-1}$ ; the SINGS IRAC images initially had  $0''.75\ \text{pixel}^{-1}$ , which we rebinned to match the other images. The Spitzer FWHM spatial resolution is  $1''.5 - 2''$  for the  $3.6\ \mu\text{m} - 8\ \mu\text{m}$  bands, and  $\sim 6''$  at  $24\ \mu\text{m}$ . For more details on the Spitzer observations and the global fluxes, see Smith et al. (2007).

We only used GALEX images with exposure times greater than 800 sec. The GALEX FUV band has an effective wavelength of  $1516\ \text{\AA}$  with a full width half maximum (FWHM) of  $269\ \text{\AA}$ , while the NUV band has an effective wavelength of  $2267\ \text{\AA}$  and FWHM  $616\ \text{\AA}$ . The GALEX images have  $1''.5$  pixels, and the point spread function has a FWHM of  $\sim 5''$ . For more details about the GALEX observations and the global fluxes, see Smith et al. (2010).

$\text{H}\alpha$  maps are available for the majority of the galaxies in our sample, either from our own observations or from published archives. We acquired new  $\text{H}\alpha$  optical images for some of the

<sup>3</sup><http://sha.ipac.caltech.edu>

galaxies using the 0.9m optical telescope of the Southeastern Association for Research in Astronomy (SARA) on Kitt Peak in Arizona<sup>4</sup> or the 4.2m William Herschel Telescope (WHT) at the Roque de los Muchachos Observatory, La Palma (Spain). These galaxies are identified in Table 1 and 2. For the SARA telescope, we used an Axiom/Apogee 2048 × 2048 CCD with binning set to 2 × 2 resulting in a pixel size of 0".51 pixel<sup>-1</sup>. For the WHT we used the ACAM (Auxiliary-port Camera; Benn, Dee, & Agócs 2008), an instrument mounted permanently at the WHT for broad-band and narrow-band imaging. The observations with ACAM resulted in a pixel size of 0.25" pixel<sup>-1</sup>. We obtained images of these galaxies in narrow-band (FWHM = 14 – 50 Å) redshifted H $\alpha$  filters matched to the redshift of the galaxy and a second narrowband image off of the H $\alpha$  line. In a few cases, a broadband red filter consistent with the SDSS r filter was used instead for the continuum. The seeing was typically 0".7 – 1".5. Continuum subtraction was accomplished as in Gutiérrez, Beckman, & Buenrasto (2011). Spectrophotometric standard stars were also observed when the sky was clear.

For most of the remaining galaxies in our sample, published continuum-subtracted H $\alpha$  maps are available from NED (see Tables 1 and 2 for references). In some cases, matching narrowband off-H $\alpha$  maps or broadband R images are available from the same source. When necessary, we registered these H $\alpha$  and continuum maps to match the Spitzer images. We used published calibration information for these images when available; otherwise, we calibrated the images using published total H $\alpha$  fluxes from Kennicutt et al. (2009). When necessary, the H $\alpha$  fluxes have been approximately corrected for the nearby [N II] lines in the filter. We assume a typical uncertainty on the H $\alpha$  fluxes of ~30%, but this likely varies from galaxy to galaxy. The total H $\alpha$  luminosity for each system is provided in Tables 1 and 2.

<sup>4</sup>The SARA 0.9m telescope at Kitt Peak is owned and operated by the Southeastern Association for Research in Astronomy (saraobservatory.org).

## 4. Clump Selection and Photometry

### 4.1. Selection

Our goal in this project is to compare the properties of star formation regions in a sample of interacting galaxies with those in normal spirals. We want to study the same physical scale within each galaxy. As a compromise between our desire for detailed spatially-resolved studies of these galaxies, the limiting resolution of the GALEX and Spitzer 24  $\mu$ m images, and our desire to have the largest sample possible, we have investigated star formation on two different physical scales within the galaxies.

First, for the entire sample of galaxies, we have selected clumps and extracted photometry using an aperture radius of 2.5 kpc. This scale is set by the limiting aperture radius of ~3".0 for accurate photometry on the GALEX and Spitzer 24  $\mu$ m images (see Section 4.3). For the most distant galaxy in our sample, Arp 107, at 142 Mpc, 2.5 kpc corresponds to 3".6. A radius of 2.5 kpc corresponds to 42".5 at the distance of the closest interacting galaxy in our sample, Arp 85 (M51), 12.1 Mpc. The closest of the spiral galaxies, NGC 7793, is at 3.28 Mpc, giving an aperture radius of 157".2.

Second, to investigate star formation on smaller scales, for a subset of galaxies we have also conducted clump selection and photometry using an aperture radius of 1.0 kpc. With a limiting aperture radius of 3".0, this subset of galaxies is limited to systems within 67 Mpc. The 1.0 kpc subset consists of 30 interacting pairs and 37 spiral galaxies. The aperture radii used for the 1.0 kpc sample range from 3".1 to 24".3.

As in our earlier studies of Arp 107, Arp 82, and Arp 285 (Smith et al. 2005; Hancock et al. 2007; Smith et al. 2008; Lapham, Smith, & Struck 2013), we selected our sample of clumps using the Spitzer 8  $\mu$ m images. Although the 24  $\mu$ m bandpass and the H $\alpha$  filter are typically considered better tracers of star formation than 8  $\mu$ m (e.g., Calzetti et al. 2005, 2007), the 24  $\mu$ m images have lower spatial resolution than the 8  $\mu$ m Spitzer images and are more likely to have artifacts, while the H $\alpha$  dataset is inhomogeneous. Further, a few of the galaxies in our sample lack 24  $\mu$ m and H $\alpha$  images. Since older stars may contribute to powering the 8  $\mu$ m emission from star form-

ing regions in some cases (Calzetti et al. 2005, 2007), some of the clumps we select may have older ages than regions selected based on  $24\ \mu\text{m}$  or  $\text{H}\alpha$ . However, more than half of the  $8\ \mu\text{m}$ -selected clumps in our earlier studies have best-fit UV/optical population synthesis ages less than 10 Myrs (Hancock et al. 2007; Smith et al. 2008; Lapham, Smith, & Struck 2013), thus we are not strongly biased against young regions.

To select clumps over a consistent spatial scale from galaxy to galaxy, we first smoothed the  $8\ \mu\text{m}$  images using a Gaussian to produce a final full width half maximum (FWHM) resolution of 2.5 kpc or 1.0 kpc, half our selected aperture diameter. For the most distant galaxies in the sample, no smoothing is needed, as this resolution is equal to the native resolution of the  $8\ \mu\text{m}$  image.

Clumps were then selected automatically from the smoothed images using the *daofind* routine (Stetson 1987) in the Image Reduction and Analysis Facility (IRAF<sup>5</sup>) software. With *daofind*, we used a detection threshold of  $10\sigma$  above the noise level in the smoothed images, and set the *sharplo*, *sharpHi*, *roundlo*, and *roundHi* parameters to 0.1, 1.2, -2.0, and 2.0, respectively, to allow slightly extended and/or elongated clumps. We visually inspected each selected source by eye, to eliminate spurious detections due to artifacts in the images.

We note that our aperture sizes are significantly larger than typical sizes of individual H II regions. For comparison, the diameter of the Orion nebula is  $\sim 5\ \text{pc}$ , while the 30 Doradus region in the Large Magellanic Cloud has a diameter  $\sim 400\ \text{pc}$ , and the giant H II regions NGC 5471 in M101 and NGC 604 in M33 have diameters of  $\sim 800\ \text{pc}$  and  $\sim 400\ \text{pc}$ , respectively (Kennicutt 1984). Thus our ‘clumps’ are likely complexes of multiple H II regions.

## 4.2. Clump Classification

We classified the clumps in the interacting galaxies into three basic groups: clumps in the inner disks of the galaxies, clumps in the tidal features, and galactic nuclei. Clumps in the spiral galaxies were classified as either nuclei or disk clumps. We used the Spitzer  $3.6\ \mu\text{m}$  images to distinguish galactic nuclei from other clumps. The

classification of clumps as ‘tidal’ vs. ‘disk’ is somewhat subjective. As in Smith et al. (2012), when the source falls inside SDSS  $g$  ( $4680\ \text{\AA}$ ) contours that have a smoothly elliptical shape, we classified it as a disk source. Alternatively, if considerable asymmetry is visible in the surrounding SDSS contours, the source is classified as tidal. Some example galaxies with their clumps marked are shown in Figure 3.

In addition to clumps associated with the galaxies, we also identified  $8\ \mu\text{m}$  point sources outside of the galaxies, which we classify as ‘off’ sources. Some of these ‘off’ sources may be detached tidally-formed star forming regions associated with the galaxies; alternatively, they may be background or foreground objects. We use these ‘off’ sources as a comparison sample for the tidal and disk objects (see Appendix). As a dividing boundary between objects classified as ‘off’ sources and ‘disk’/‘tidal’ sources assumed to be associated with the galaxies, for the galaxies with SDSS images available we use an SDSS  $g$  filter isophote of  $24.58\ \text{mag/arcsec}^2$ . This is approximately equivalent to  $B = 25\ \text{mag/arcsec}^2$ , using the median  $g - r$  color for tidal tails from Smith et al. (2010) and the Jester et al. (2005)  $g$  to  $B$  conversion.

For systems with no SDSS images available, we use a GALEX NUV surface brightness of  $26.99\ \text{mag/arcsec}^2$ , applying the median NUV -  $g$  color of tidal tails of 2.4 (Smith et al. 2010). For the three systems with neither SDSS nor GALEX images, we used a Spitzer  $3.6\ \mu\text{m}$  isophote of  $20.91\ \text{mag/arcsec}^2$ , using the median  $g - [3.6]$  color of 3.67 for tidal tails (Smith et al. 2007, 2010). Some of the sources we list as ‘disk’ and ‘tidal’ may not be physically associated with the galaxies, but instead may be foreground or background objects. This topic is discussed further in Section 4.5 and the Appendix.

In the interacting galaxy 1.0 kpc clump sample, there are 514 disk clumps, 208 tidal clumps, and 162 ‘off’ clumps, in addition to the 60 nuclear regions. In the 1.0 kpc radius clump sample for the spiral galaxies, there are 997 disk clumps and 85 ‘off’ regions, as well as 37 nuclear regions. The 2.5 kpc clump sample for the interacting galaxies has 151 disk clumps, 252 tidal regions, and 190 ‘off’ sources, along with 92 nuclear sources. There are 159 disk clumps in the 2.5 kpc radius clump

<sup>5</sup><http://iraf.noao.edu>

sample for the spiral galaxies, along with 51 ‘off’ sources and 39 nuclei.

### 4.3. Photometry

From the Spitzer, GALEX, and  $H\alpha$  images, we extracted aperture photometry of the clumps from the unsmoothed images using the IRAF *phot* routine. As noted above, for this photometry we use radii of either 2.5 kpc or 1.0 kpc, depending upon the sample. We used a sky annulus with the mode sky fitting algorithm, with an inner radius equal to the aperture radius, and an annulus width equal to  $1.2 \times$  the aperture radius. The mode option for determining the background is useful in crowded fields.

For the more distant galaxies in the sample, aperture corrections are needed to account for flux spillage outside of the aperture. This is particularly important for the GALEX and Spitzer 24  $\mu\text{m}$  images, which are relatively low spatial resolution; however, we also utilize aperture corrections for the Spitzer IRAC images. For the  $H\alpha$  photometry, we did not apply aperture corrections since these corrections are expected to be small. For the Spitzer images, we used aperture corrections from the IRAC and MIPS Instrument Handbooks<sup>6</sup>, interpolating between the tabulated values. For the GALEX images, we calculated aperture corrections for each image individually, by doing aperture photometry for three to ten moderately bright isolated point sources in the field. For these stars, we extracted the fluxes within our target apertures, and compared with that obtained using a  $17''$  radius. No aperture corrections were used for GALEX for aperture radii  $\geq 17''$ . If the clumps are somewhat resolved at these spatial scales, then aperture corrections based on stars in the field will be under-estimates. The aperture corrections for the GALEX bands are plotted against aperture radius in Figure 4. Note that the NUV aperture corrections are more consistent from image to image than those at FUV.

We corrected the UV photometry for Galactic reddening by starting with optical estimates from Schlafly & Finkbeiner (2011) as provided by NED, and extrapolating to the UV using the Cardelli, Clayton, & Mathis (1989) attenuation law.

### 4.4. Fraction Global Light in Clumps

For each galaxy in the sample, we co-added the fluxes for the clumps in that galaxy, and compared the combined light of the clumps with the global fluxes of the galaxies as tabulated in Smith et al. (2007, 2010) and Smith & Struck (2010). The fraction of the total light from the galaxy due to the targeted clumps varies from galaxy to galaxy and wavelength to wavelength. On average for all wavelengths, the fraction of the total light in clumps is about 20% higher for the 2.5 kpc clump sample than for the 1.0 kpc clump sample. At 8  $\mu\text{m}$  for the 1.0 kpc sample, the median fraction in clumps is 27% for the spirals and 34% for the interacting galaxies. For the 2.5 kpc sample, the median fraction in clumps at 8  $\mu\text{m}$  is 38% for the spirals and 58% for the interacting galaxies. Within these samples, there is a large scatter from galaxy to galaxy, likely depending upon the sensitivity of the image, the morphology of the galaxy, and the age of the regions. Similar fractions are found for the FUV and  $H\alpha$  images, while the NUV images have smaller fractions on average (median fractions in clumps between 17% and 42%, depending upon the sample). At 24  $\mu\text{m}$ , the median fraction in clumps is about 60% higher on average than at 8  $\mu\text{m}$ . These results are consistent with a picture in which the NUV light originates from older more dispersed stars than the stars traced in the other bands, while the 24  $\mu\text{m}$  light is powered by younger more embedded stars which are more confined to the clumps.

For all wavelengths, the interacting galaxies have larger fractions in clumps than the spirals. On average, the median fractions for the interacting galaxies are about a factor of 1.7 times larger than those in the spirals. This suggests that the star forming regions in the interacting galaxies are more luminous, dustier, or younger on average than those in the spirals, so are easier to detect at 8  $\mu\text{m}$ . The difference in the clump fraction is likely not due to sensitivity differences, as the 8  $\mu\text{m}$  images of the spirals are on average more sensitive to lower luminosity clumps than those of the interacting galaxies (see Figures 7 and 8).

### 4.5. Background/Foreground Sources

Some of the objects classified as ‘disk’ or ‘tidal’ may actually be foreground stars, background

<sup>6</sup><http://irsa.ipac.caltech.edu/data/SPITZER/docs/>



quasars, or background galaxies. There are three ways to distinguish such objects. First, if an optical spectrum is available for the source, the redshift of the clump can be used to confirm its association with the galaxy. Unfortunately, for only a handful of the clumps are optical spectra available, mainly galactic nuclei.

Second, a detection in the  $H\alpha$  map would confirm it is at the same redshift as the galaxy, thus likely associated with the galaxy. Unfortunately, however,  $H\alpha$  images are not available for all of the galaxies in our sample. Even when an  $H\alpha$  map is available, it may not be sensitive enough to detect all of the star forming regions in the galaxy, particularly those that are highly obscured and/or low luminosity.

A third way to identify foreground or background interlopers is via their position in Spitzer infrared color-color plots (Smith et al. 2005; Lapham, Smith, & Struck 2013). Foreground stars have near-to-mid-infrared spectral energy distributions (SEDs) that drop with increasing wavelength, star forming regions have SEDs that drop from  $3.6\ \mu\text{m}$  to  $4.5\ \mu\text{m}$  and then increase at longer wavelengths, and quasars have flat SEDs in this wavelength range. The application of this method to our clump sample is described in detail in the Appendix to this paper.

## 5. Clump Star Formation Rates

### 5.1. Calculating SFRs

For both the 2.5 kpc and 1.0 kpc samples, we made six different estimates of the SFR of each clump. For clumps detected ( $\geq 3\sigma$ ) in both the FUV and  $24\ \mu\text{m}$  filters, we made a first estimate of the star formation rate,  $\text{SFR}_{FUV+24}$ , by correcting the FUV luminosity  $L_{FUV}$  for extinction using  $L_{FUV}(\text{corrected}) = L_{FUV} + 6.0L_{24}$  and then using the relation  $\text{SFR}_{FUV+24} = 3.39 \times 10^{-44} L_{FUV}(\text{corr})$  (Leroy et al. 2008; Liu et al. 2011).<sup>7</sup> In these formulae, the SFR is in units of  $M_{\odot}\ \text{yr}^{-1}$  and the luminosities are monochromatic

luminosities ( $\nu L_{\nu}$ ) in  $\text{erg s}^{-1}$ .

For systems with both NUV and  $24\ \mu\text{m}$  measurements, we obtained a second estimate  $\text{SFR}_{NUV+24}$  by correcting the NUV for extinction using  $L_{NUV}(\text{corr}) = L_{NUV} + 2.26L_{24}$  and then using  $\text{SFR}_{NUV+24} = 6.76 \times 10^{-44} L_{NUV}(\text{corr})$  (Hao et al. 2011; Kennicutt & Evans 2012).

Third, for the clumps detected in  $H\alpha$  and at  $24\ \mu\text{m}$ , we obtain another estimate of the SFR using the equation  $\text{SFR}_{H\alpha+24} = 5.5 \times 10^{-42} [L_{H\alpha} + 0.031 L_{24}]$ . This relationship was found for H II regions in nearby galaxies assuming a Kroupa initial mass function (Calzetti et al. 2007; Kennicutt et al. 2009).

Our fourth estimate of the SFR was obtained from the  $24\ \mu\text{m}$  photometry alone, using  $\text{SFR}_{24} = 2.0 \times 10^{-43} L_{24}$  (Rieke et al. 2009). This is especially valuable for systems without NUV, FUV, and  $H\alpha$  images.

For systems with both NUV and  $8\ \mu\text{m}$  images, we make a fifth estimate of the SFR,  $\text{SFR}_{NUV+8}$ , by using  $L_{NUV}(\text{corr}) = L_{NUV} + 1.24L_8$ . We obtained this relation by combining the  $8\ \mu\text{m}$  and  $24\ \mu\text{m}$  relations of Kennicutt et al. (2009). Finally, we obtained a sixth estimate of the SFR from the  $8.0\ \mu\text{m}$  luminosity alone, using  $\text{SFR}_8 = 1.63 \times 10^{-43} L_8$ , after using the  $3.6\ \mu\text{m}$  luminosity  $L_{3.6}$  to correct for contributions to the  $8\ \mu\text{m}$  flux from starlight from the  $3.6\ \mu\text{m}$  flux with  $F_8(\text{starlight}) = 0.26F_{3.6}$  (Wu et al. 2005).

The derived SFRs are a measure of the extinction-corrected  $H\alpha$  luminosities of the clumps, and therefore the number of ionizing photons in the region. The SFR equations given above depend upon the assumed dust attenuation law, which depends upon the dust distribution relative to the UV-emitting stars and the ionized gas. This issue is discussed further in Section 6.

These estimates of SFR also depend upon the star formation history for the region. These formulae were derived assuming constant star formation rates over the last  $\sim 10 - 100\ \text{Myrs}$  (see Kennicutt & Evans 2012), while the clumps have probably undergone recent bursts of star formation. They are particularly uncertain for low luminosity clumps, when stochastic effects can be important. In spite of these limitations and uncertainties, however, these numbers aid comparison to other studies, which frequently

<sup>7</sup>Note that Hao et al. (2011) derive a somewhat different relationship:  $\text{SFR}_{FUV+24} = 5.0 \times 10^{-44} L_{FUV}(\text{corr})$  and  $L_{FUV}(\text{corr}) = L_{FUV} + (3.89 \pm 0.15)L_{24}$  (see also Kennicutt & Evans 2012). The Hao et al. (2011) conversion is intended for the global fluxes of galaxies, while the Leroy et al. (2008) and Liu et al. (2011) relation is for spatially-resolved studies (C. Hao 2015, private communication).

quote SFRs for individual knots of star formation within galaxies (e.g., Boquien et al. 2007, 2009b, 2011; Kennicutt et al. 2007; Cao & Wu 2007; Beirão et al. 2009; Pancoast et al. 2010; Smith et al. 2014) as well as galaxies as a whole (e.g., Kennicutt & Evans 2012).

In general, the reliability of the SFR tracers given above depends upon the band or bands used. In the following analysis, we use  $\text{SFR}_{FUV+24}$  as our preferred estimate of the SFR when it is available (36/46 interacting galaxies; 31/39 spirals). If it is not available, in order of preference we use  $\text{SFR}_{NUV+24}$  (4 interacting and 3 spiral galaxies),  $\text{SFR}_{H\alpha+24}$  (4 interacting and 1 spiral),  $\text{SFR}_{24}$  (1 interacting and 1 spiral),  $\text{SFR}_{NUV+8}$  (1 interacting and 3 spirals), and  $\text{SFR}_8$  (no interacting and no spirals). In general, the 24  $\mu\text{m}$  flux is considered a better tracer of star formation than 8  $\mu\text{m}$ . The 24  $\mu\text{m}$  light from galaxies is dominated by emission from ‘very small interstellar dust grains’ heated mainly by UV light from massive young stars (e.g., Li & Draine 2001). In contrast, the 8  $\mu\text{m}$  flux in star forming galaxies may be powered in part by older stars. The 8  $\mu\text{m}$  luminosity is not linearly proportional to estimates of star formation from the near-infrared hydrogen Pa $\alpha$  line, unlike the 24  $\mu\text{m}$  luminosity (Calzetti et al. 2005, 2007). Further, since the 8  $\mu\text{m}$  broadband Spitzer flux from galaxies is dominated by spectral features produced by polycyclic aromatic hydrocarbons (PAHs) (Li & Draine 2001), this flux can vary with metallicity, with low metallicity regions being particularly deficient in the 8  $\mu\text{m}$  band compared to 24  $\mu\text{m}$  (Boselli et al. 1998; Engelbracht et al. 2005; Rosenberg et al. 2006, 2008). Thus SFR tracers using 24  $\mu\text{m}$ , if available, are preferred to those using 8  $\mu\text{m}$ . Likewise, tracers using the FUV are preferred over those using the NUV, since older stars contribute more to the NUV light (e.g., Kennicutt & Evans 2012).  $H\alpha + 24 \mu\text{m}$  is generally considered a very reliable measure of star formation (e.g., Kennicutt et al. 2009). However, we rank  $\text{SFR}_{H\alpha+24}$  lower in preference than estimates using the FUV or NUV with 24  $\mu\text{m}$  because our  $H\alpha$  data are inhomogeneous, being obtained from a variety of sources. Using either UV or  $H\alpha$  in addition to 24  $\mu\text{m}$  is considered more accurate than 24  $\mu\text{m}$  alone, because extincted and unextincted young stars are both directly accounted for (e.g., Kennicutt et al. 2009). Thus 24  $\mu\text{m}$  alone is

only used when UV or  $H\alpha$  measurements are not available. Only when no alternative is available do we use the 8  $\mu\text{m}$  alone as our indicator of the SFR.

In Figures 5 and 6, we plot various ratios of the different measures of star formation against SFR. These plots indicate reasonably good consistency between the different methods of determining SFR, but with some scatter. Some of the scatter in Figures 5 and 6 is likely due to how the different SFR tracers depend upon properties of the region such as age, star formation history, dust composition, extinction, geometry, and initial mass function. For example, FUV is skewed towards younger stars than the NUV, and the UV is more sensitive to the assumed dust properties than  $H\alpha$ . Note that there is a slight anti-correlation between  $\text{SFR}_{NUV+24}/\text{SFR}_{FUV+24}$  and SFR. This may be due to clump-to-clump age variations, with younger ages giving both lower  $\text{SFR}_{NUV+24}/\text{SFR}_{FUV+24}$  and higher SFRs. Alternatively, the attenuation correction may vary with SFR. For low luminosity regions, stochastic variations from region to region due to random sampling of the initial mass function may also play a role, however, this is not a factor for the high SFR regions.

Our ranking of the various tracers of SFR is supported by Figures 5 and 6. Moderate scatter is seen for the ratio  $\text{SFR}_{NUV+24}/\text{SFR}_{FUV+24}$ , showing that these two methods give reasonably consistent SFRs. In contrast, large scatter is seen for  $\text{SFR}_{NUV+8}/\text{SFR}_{FUV+24}$  and  $\text{SFR}_8/\text{SFR}_{FUV+24}$ , supporting the assertion that 8  $\mu\text{m}$ , with or without UV, is a less reliable indicator of SFR. Ratios involving  $H\alpha$  also show moderate scatter. The  $\text{SFR}_{24}/\text{SFR}_{NUV+24}$  ratios are skewed towards values less than one, likely because unobscured young stars are not being included in the census in  $\text{SFR}_{24}$ .

We note that the above SFR relations depend upon metallicity, especially those involving the 8  $\mu\text{m}$  flux, particularly at oxygen abundances less than  $\log(\text{O}/\text{H}) + 12 = 8.4$  (Calzetti et al. 2007). No abundance determinations are available for most of the star forming regions in our sample. In most cases, however, they are likely to be higher than this limit. For example, the tidal features in Arp 72, Arp 105, and Arp 245 have  $\log(\text{O}/\text{H}) + 12 = 8.7, 8.6, \text{ and } 8.65$ , respectively (Smith et al.

2010; Duc & Mirabel 1994; Duc et al. 2000).

## 5.2. Histograms of SFRs

Figure 7 displays histograms of the SFRs of the clumps obtained with a 2.5 kpc radius aperture. These histograms are proxies for the extinction-corrected  $H\alpha$  luminosity functions of the regions. The top panel in Figure 7 shows the disks and tidal clumps in the interacting galaxies, while the disk clumps of the spiral galaxies are given in the second panel. The hatched histogram in the top panel indicates the tidal clumps. Similar histograms for the 1.0 kpc radius clumps are provided in Figure 8.

Note that Figures 7 and 8 do not include the ‘nuclear clumps’, just the extranuclear ‘disk’ and ‘tidal’ regions. The fluxes from the nuclear regions may be contaminated by active galactic nuclei. In addition, the stellar populations in the nuclear and immediate circumnuclear regions may differ from those in star forming regions further out in the disk. For example, circumnuclear rings may have long star formation histories in comparison to regions further out in the disk (e.g., Kennicutt, Keel, & Blaha 1989; Sarzi et al. 2007; Dors et al. 2008). In our sample galaxies, such circumnuclear rings (for example, in NGC 1097 and NGC 4321) are contained within the ‘nuclear clumps’, thus do not contribute to Figures 7 and 8.

Along the top axes of Figures 7 and 8, we converted the SFRs into SFR per area by dividing by the area per aperture (19.6 kpc<sup>2</sup> for the 2.5 kpc aperture radii regions and 3.14 kpc<sup>2</sup> for the 1.0 kpc aperture radii clumps). In these plots, the red histograms mark the clumps that are detected in  $H\alpha$ , and thus are confirmed to be associated with the galaxies. In the blue histograms, we identify the clumps that are *either* detected in  $H\alpha$  or do *not* lie in the stellar or quasar areas in the Spitzer color plots, or both (see Appendix). In other words, clumps not included in the blue histogram are likely *not* associated with the galaxies. Clumps in the blue histogram but not in the red histogram may be part of the galaxies, but that is uncertain.

In all cases, the histograms of SFRs are centrally peaked. The drop off in the number of clumps with lower luminosity may be due in part

to incompleteness. We did two calculations to estimate the completeness limit of the sample. First, for the smoothed 8  $\mu$ m images, we calculated the theoretical sensitivity to point sources, based on the  $10\sigma$  clump selection criteria used by *daofind*. Histograms of these limits, after conversion to SFR, are given in the lower two panels in Figures 7 and 8, for the 2.5 kpc and 1.0 kpc samples, respectively. The y-axes on these lower histograms are the logarithm of the number of galaxies with each sensitivity. Figures 7 and 8 show that the turn-over in the luminosity function is significantly higher than the theoretical  $10\sigma$  sensitivity limit for the images.

However, crowding of clumps may lead to blending and therefore incompleteness. To test for this, we used the IRAF *mkobjects* routine to randomly add artificial clumps to the disks of the galaxies in our smoothed 8  $\mu$ m images. We then determined how many of these sources were recovered by *daofind*. For the 1.0 kpc radius clump sample, we find the sample is 74% complete at a SFR = 0.025  $M_{\odot} \text{ yr}^{-1}$ , 80% complete at a SFR = 0.04  $M_{\odot} \text{ yr}^{-1}$ , 90% complete at a SFR = 0.1  $M_{\odot} \text{ yr}^{-1}$ , and 95% complete at a SFR = 0.25  $M_{\odot} \text{ yr}^{-1}$ . For the 2.5 kpc sample, we find an estimated 53% completeness at 0.16  $M_{\odot} \text{ yr}^{-1}$ , 60% completeness at 0.25  $M_{\odot} \text{ yr}^{-1}$ , 70% at 0.4  $M_{\odot} \text{ yr}^{-1}$ , and 85% at SFR = 1  $M_{\odot} \text{ yr}^{-1}$ .

For both samples of clumps, we fit the high SFR end of the log N - log SFR distribution to a straight line, where N is the number of clumps in a luminosity bin and the width of the bin scales with log(SFR) as in Figures 7 and 8. For the 2.5 kpc samples, we only fit the distribution above log(SFR) > -0.8 (SFR > 0.16  $M_{\odot} \text{ yr}^{-1}$ ), above the point where the distribution function turns over. For the 1.0 kpc sample, we used a cut-off of log(SFR) > -1.4 (SFR > 0.04  $M_{\odot} \text{ yr}^{-1}$ ). For these fits, we only included the data within the blue histograms, thus we are eliminating the most likely foreground/background interlopers from the sample. Adding the excluded sources back in the sample doesn’t change the results significantly, since very few of the sources above our cutoffs lie in the stellar or quasar area of the Spitzer color-color plot.

The best-fit slopes of these lines are provided in Figures 7 and 8. For the 2.5 kpc sample, we find a slope of  $-0.79 \pm 0.14$  for the interacting

galaxies and  $-1.01 \pm 0.15$  for the spiral galaxies. For the 1.0 kpc sample, the slope is  $-0.92 \pm 0.06$  for the interacting galaxies and  $-1.54 \pm 0.13$  for the spiral galaxies. For both samples of clumps, the distribution of SFR is flatter for the interacting clumps than for the spiral clumps, that is, there are proportionally more high SFR clumps in the interacting galaxies than in the spirals (Figures 7 and 8). For the 2.5 kpc sample, a Kolmogorov-Smirnov test on the distribution of clumps above  $\log(\text{SFR}) > -0.8$  ( $\text{SFR} > 0.16 \text{ M}_\odot \text{ yr}^{-1}$ ) gives a probability of 2% that the two sets of clumps come from the same parent sample. For the 1.0 kpc sample, using a Kolmogorov-Smirnov test on the distribution above  $\log(\text{SFR}) > -1.4$  ( $\text{SFR} > 0.04 \text{ M}_\odot \text{ yr}^{-1}$ ) gives a probability of 1.6% that the interacting and spiral clumps come from the same parent sample.

To test whether systematic differences between the various SFR indicators (Figures 5 and 6) affects these conclusions, we repeated this analysis using a different order of preference for the SFR indicators. In this second analysis, we used  $\text{SFR}_{H\alpha+24}$  as the top choice if available, followed by  $\text{SFR}_{NUV+24}$ ,  $\text{SFR}_{FUV+24}$ ,  $\text{SFR}_{24}$ ,  $\text{SFR}_{NUV+8}$ , and  $\text{SFR}_8$  in order. We then fit the high SFR end of the SFR distribution to power laws as in Figures 7 and 8. For the 2.5 kpc sample, we find a slope of  $-0.64 \pm 0.37$  for the interacting galaxies and  $-0.82 \pm 0.24$  for the spiral galaxies. For the 1.0 kpc sample, the slope is  $-0.90 \pm 0.09$  for the interacting galaxies and  $-1.45 \pm 0.18$  for the spiral galaxies. These are consistent with the results found for the original priority ordering scheme though with larger uncertainties.

The results shown in Figures 7 and 8 imply that there are more young stars, on average, per region in the interacting galaxies (i.e., a higher density of stars). This means that either the efficiency of star formation per region is higher in interacting galaxies, or there is more interstellar gas per clump, or both. This issue is discussed further in Section 6.3.

An alternative explanation for the higher SFRs for the clumps in the interacting galaxies is that clumps are ‘blended’ together more frequently in the interacting galaxies, which are more distant on average. However, we are extracting the photometry over the same physical scale in all of the galaxies, so the relative amount of blending should

be similar in the two samples, unless star forming regions are closer together on average in the interacting galaxies or more frequently aligned along our line of sight in the interacting galaxies due to the tidal interaction. One argument against blending alone being responsible for the difference between the two samples comes from high resolution Hubble Telescope images of the highest SFR regions. As discussed in Smith et al. (2014) and summarized in Section 5.3 of the current paper, at high resolution the most luminous clumps in our sample are seen to contain extremely luminous star clusters at their core.

For a 2.5 kpc radius aperture clumps, the slope of the tidal clumps in the interacting galaxies (the hatched histogram in Figure 7) show a flatter distribution than the disk clumps in the interacting galaxies, indicating that the highest SFR regions are preferentially tidal. However, this is uncertain because the classification of ‘disk’ vs. ‘tail’ is quite ambiguous. In contrast, most of the highest SFR regions in the 1.0 kpc sample are classified as disk sources (Figure 8). As discussed below, the distance-limited 1.0 kpc sample lacks some of the most extreme regions (i.e., the hinge regions in Arp 240 and Arp 256).

### 5.3. The Highest SFR Clumps

A comparison of the top and bottom panels in Figures 7 and 8 shows that the most luminous clumps are found in the interacting galaxies. On a 2.5 kpc radius scale (Figure 7), no clumps are found in the spiral sample with  $\text{SFR} \geq 2 \text{ M}_\odot \text{ yr}^{-1}$ , while five such clumps are found in the interacting sample. These include three hinge clumps in Arp 240 (3.3, 6.2, and  $9.0 \text{ M}_\odot \text{ yr}^{-1}$ ), the ‘overlap region’ between the two disks of the Antennae galaxies Arp 244 ( $4.8 \text{ M}_\odot \text{ yr}^{-1}$ ), and the hinge clump in Arp 256 ( $2.0 \text{ M}_\odot \text{ yr}^{-1}$ ). A knot of star formation near the base of the short western tail of NGC 2207 has a slightly lower SFR of  $1.8 \text{ M}_\odot \text{ yr}^{-1}$ . These regions and their host galaxies are discussed in detail in Smith et al. (2014).

Hubble Telescope images reveal extremely luminous star clusters ( $M_I$  between  $-12.2$  and  $-16.5$ ) at the centers of the Arp 256, Arp 240, and NGC 2207 clumps (Smith et al. 2014). These clusters are resolved with HST with estimated sizes of  $\sim 70$  pc, much larger than most luminous star clusters (e.g., Larsen 2004). If individual star clusters,

their luminosities would place them near the top of the luminosity function for extragalactic star clusters (e.g., Gieles 2010). These sources may actually be tightly packed groups of star clusters, rather than individual clusters. HST images of the more nearby Antennae galaxies shows tightly grouped complexes of star clusters in the overlap region (Whitmore et al. 2010). If smoothed to the effective resolution of Arp 240 and Arp 256, these clusters would be blended together to produce a source similar in size and luminosity to the sources seen in those galaxies (Smith et al. 2014). Alternatively, these sources may be single very large clusters. Numerical simulations of star cluster formation and evolution in galaxy interactions indicate that large clusters can be produced by either cluster mergers, mergers of gas clouds, or expansion due to a passage through the inner disk of the galaxy (Fellhauer & Kroupa 2005; Renaud et al. 2014).

In an early study, Kennicutt & Chu (1988) found that some of the largest H II regions in nearby galaxies host unusually luminous star clusters. Later studies have indicated that the global star cluster formation efficiency in galaxies (the fraction of star formation occurring in dense bound star clusters) increases as the star formation rate of the galaxy increases (Goddard, Bastian, & Kennicutt 2010; Adamo, Östlin, & Zackrisson 2011; Adamo et al. 2015). Locally within galaxies this trend is also seen, along with a trend towards higher cluster formation efficiency in regions with higher gas surface density (Ryon et al. 2014; Adamo et al. 2015). Theoretical models (Elmegreen 2008; Kruijssen 2012) predict such a trend, as regions with higher gas density have shorter free-fall times and higher star formation efficiencies, thus are less affected by gas expulsion and so are more likely to form dense bound clusters. Our observation of very luminous clusters or dense clusters of clusters in the clumps with the highest SFRs may be consistent with this trend.

Another intriguing difference between the highest SFR knots and those in normal spiral galaxies comes from Chandra X-ray images. In Chandra maps, the highest SFR regions tend to have strong diffuse X-ray emission with a soft spectrum, indicative of hot gas (Smith et al. 2014). The diffuse  $L_X$ /SFR ratios for the highest SFR

clumps are higher than those for regions in normal spirals, suggesting higher density gas on average (Smith et al. 2014). This is consistent with a picture in which large quantities of gas are being driven into these regions.

In the spiral sample at the 2.5 kpc radius scale, only two clumps have SFRs greater than  $1 M_\odot \text{ yr}^{-1}$ . These both lie in the outer spiral arms of NGC 3646, and have inferred SFRs of 1.2 and  $1.5 M_\odot \text{ yr}^{-1}$  (see Figure 9). Although it is in our control sample of ‘normal’ spiral galaxies, NGC 3646 does have a companion, NGC 3649, which has a blue luminosity of  $1/24^{\text{th}}$  that of NGC 3646 (from NED). This is just below the cut-off used by Smith et al. (2007, 2010) to eliminate interacting galaxies from the control sample. Thus NGC 3646 is interacting, though not as strongly as the systems in the SB&T sample. Interestingly, the most luminous clumps in NGC 3646 lie near where spiral arms appear to cross, with a morphology suggestive of intersecting caustics. Thus at least some of the star formation that is occurring in our control sample was likely also triggered by interactions. Numerical simulations of flyby encounters between galaxies shows that low mass companions ( $0.01 - 0.1 \times$  the mass of the primary) can induce long-lived tidal waves in galaxies (Struck, Dobbs, & Hwang 2011).

NGC 3646 has been identified as being one of the largest and most luminous spirals in the local Universe (van den Bergh 1960; Romanishin 1983), with a  $D_{25}$  diameter (de Vaucouleurs et al. 1991) of 74 kpc at a distance of 65 Mpc. Thus even if it was not interacting it would be a likely host for luminous star forming regions. For spiral galaxies of a given Hubble type, the luminosities of the brightest H II regions scale with the luminosity of the galaxy as a whole (Kennicutt 1988). NGC 3646 has the 3rd largest  $3.6 \mu\text{m}$  luminosity of the spiral galaxies in our sample (see Figure 2).

As discussed in Section 4, due to resolution issues the 1.0 kpc sample of clumps is limited to galaxies within 67 Mpc. That means that two of the galaxies with the most luminous clumps in the 2.5 kpc sample, Arp 240 and Arp 256, are not included in the 1.0 kpc clump sample. However, Figure 8 shows that even without these more distant systems there is a difference between interacting and normal galaxies. On a 1.0 kpc radius scale, interacting galaxies host proportionally

more clumps with  $\log(\text{SFR}) > -0.6$  ( $\text{SFR} > 0.25 \text{ M}_{\odot} \text{ yr}^{-1}$ ) compared to the spiral galaxies (Figure 8).

In the 1.0 kpc sample, the clump with the highest SFR is the overlap region in the Antennae galaxies Arp 244. The two NGC 3646 clumps are the most luminous in the spiral sample. The derived luminosities of these clumps are similar with the two aperture sizes, indicating that the star formation is compact relative to the 2.5 kpc radius aperture.

#### 5.4. Comparison to Earlier Studies

In a now classic paper, Kennicutt, Edgar, & Hodge (1989) derived  $\text{H}\alpha$  luminosity functions of HII regions in a sample of nearby spiral and irregular galaxies on scales of 100 – 200 pc. They found a trend with Hubble type, with flatter luminosity functions for the Sm – Im galaxies than for Sab – Sb galaxies on average, with Sbc and Sc in between. Our best-fit slope for the 1.0 kpc sample of clumps in our interacting galaxies is consistent with their results for their Sm – Im galaxies, while our best-fit value for our spiral clumps is in the range for their spirals (note that they fit  $dN/dL = AL^{\alpha}$ , while we fit to  $dN/d(\log(L))$ , thus our slope  $= \alpha + 1$ ). Our 2.5 kpc sample for the interacting galaxies gives a slope between that of the Sm – Im galaxies and the spirals, while the slope for the 2.5 kpc spiral sample is similar to that of early-type spirals.

In a recent study, Zaragoza-Cardiel et al. (2015) use  $\text{H}\alpha$  Fabry-Perot data to derive  $\text{H}\alpha$  luminosities and velocity dispersions for H II regions in 12 galaxies in nine interacting systems, and compared with 28 isolated galaxies. Similar to our results, they found a flatter H II region luminosity function for the interacting systems than for the normal galaxies. Their study involved smaller spatial scales than ours (the diameters of their regions ranged from 15 – 400 pc) and their  $\text{H}\alpha$  fluxes were uncorrected for attenuation, but the slopes they found for the high luminosity end of their luminosity functions are similar to ours.

## 6. Dust Attenuation

### 6.1. Dust Attenuation vs. SFR

In Figures 10, 11, and 12, we compare the SFRs of the clumps against three standard indicators of dust extinction: the  $L_{\text{H}\alpha}/L_{24}$  ratio, the NUV – [24] color, and the FUV – [24] color, respectively. In these plots, the 2.5 kpc radius clumps are shown in the top panel, and the 1.0 kpc radius clumps in the bottom. In all cases, we see a trend, such that the higher SFR clumps have more dust absorption.

The best linear fits to the datapoints are shown in Figures 10, 11, and 12 as solid blue lines. Inspection of these plots shows that the trends are not exactly linear, but are flatter at the low SFR end, steepening at higher SFR. Note that there is quite a bit of scatter about the best-fit lines, particularly for the 1.0 kpc scale clumps, for which no correlation is visible if clumps with  $\log \text{SFR} > -1.4$  ( $\text{SFR} > 0.04 \text{ M}_{\odot} \text{ yr}^{-1}$ ) are excluded. On average, the clumps in the spiral galaxies have less dust absorption than those in the interacting galaxies, but follow the same general trend.

The observed correlations between SFR and implied dust attenuation may occur because regions with higher gas column densities have higher dust column densities, and higher gas column densities produce higher SFRs. The latter relationship has been quantified in the so-called Schmidt-Kennicutt Law (Schmidt 1959; Kennicutt 1989, 1998), in which the SFR surface density  $\Sigma_{\text{SFR}}$  is related to the surface density of the interstellar gas  $\Sigma_{\text{gas}}$  via a power law. This relation is discussed further in Section 6.3.

A correlation between the apparent UV attenuation of star forming regions and their luminosity was found before by Boquien et al. (2009). They extracted GALEX FUV and Spitzer 24  $\mu\text{m}$  fluxes for regions within eight nearby spiral galaxies, using a spatial scale of  $\sim 300$  pc. They found that  $L_{24}$  increases at a faster rate than  $L_{\text{FUV}}$ , consistent with our Figure 12.

### 6.2. Dust Attenuation Laws

In Figure 13, we compare our three indicators of dust attenuation against each other. Again, the datapoints are color-coded as open black squares for the disk clumps in the interacting galaxies, magenta open diamonds for the tidal clumps, and

small blue filled triangles for clumps in the disks of the spirals. Regions with SFRs greater than  $0.4 \text{ M}_{\odot} \text{ yr}^{-1}$  have a green circle around them. In general, the three tracers of attenuation correlate with each other, though with significant scatter. The observed trends in these plots provide us with a measure of the average attenuation law in these regions, while the observed scatter around the average trends is likely due to variations in the geometry, age, and dust properties of the clumps. In Figure 13, the solid magenta lines show the best linear fits to the data for all of the clumps, while the green dotted lines are the best-fit lines for the clumps with  $\text{SFR} > 0.4 \text{ M}_{\odot} \text{ yr}^{-1}$ .

The high SFR clumps trace out a steeper path in Figure 13 than the full sample of clumps. This implies that for the high SFR clumps, for a given change in the observed  $\text{H}\alpha$ , the UV changes more, compared to lower luminosity clumps. This may be due to a steeper UV-to- $\text{H}\alpha$  dust attenuation curve in high SFR clumps than in lower luminosity clumps. Alternatively, it may be caused by age differences between the clumps. These possibilities are discussed further below.

Our dataset can be used to estimate the relative dust attenuation in the  $\text{H}\alpha$  and UV filters. A standard technique for deriving dust attenuation laws is the ‘SFR matching’ method, as outlined by Hao et al. (2011) (also see Buat et al. 2002, Treyer et al. 2007 and Boquien et al. 2015). This starts with the generic formula for the SFR based on the UV, NUV, or  $\text{H}\alpha$  luminosities as used in Section 5.1:

$$\text{SFR} = C_{\lambda} L_{\lambda}(\text{corrected})$$

where  $L_{\lambda}(\text{corrected})$  is the luminosity in the band after correction for attenuation, and  $C_{\lambda}$  is the conversion factor to SFR for that band.  $L_{\lambda}(\text{corr})$  is then equal to  $L_{\lambda}(\text{observed})10^{0.4A_{\lambda}}$ , where  $A_{\lambda}$  is the effective attenuation in that band in magnitudes. We then assume that the  $\text{H}\alpha$  attenuation obtained using the formula for  $\text{SFR}_{\text{H}\alpha+24}$  given in Section 5.1 is reliable:  $A_{\text{H}\alpha} = 2.5\log(1 + 0.031L_{24}/L_{\text{H}\alpha})$  (from Calzetti et al. 2007 and Kennicutt et al. 2009).<sup>8</sup>

<sup>8</sup>We note that Zhu et al. (2008) find  $A_{\text{H}\alpha} = 2.5\log(1 + 0.020L_{24}/L_{\text{H}\alpha})$ . As discussed in Zhu et al. (2008) and Kennicutt et al. (2009), the Zhu et al. (2008) formula is for galaxies as a whole, while the Calzetti et al. (2007) relation is for spatially-resolved observations.

We then set the SFRs derived from other filters equal to that from the corrected  $\text{H}\alpha$ , i.e.:

$$\text{SFR}_{\lambda} = \text{SFR}_{\text{H}\alpha}(\text{corr}),$$

$$\text{where } \text{SFR}_{\text{H}\alpha}(\text{corr}) = C_{\text{H}\alpha} L_{\text{H}\alpha}(\text{obs})10^{0.4A_{\text{H}\alpha}}.$$

Rearranging and plugging in  $\lambda = \text{FUV}$  gives:

$$\log(L_{\text{H}\alpha}/L_{\text{FUV}})(\text{observed}) = 0.4(A_{\text{FUV}}/A_{\text{H}\alpha} - 1)A_{\text{H}\alpha} - \log(C_{\text{H}\alpha}/C_{\text{FUV}})$$

According to the above formula, if  $A_{\text{FUV}}/A_{\text{H}\alpha}$  does not vary from clump to clump and the SFR matching technique is valid for these regions, the slope of the best-fit line in a plot of  $\log(L_{\text{H}\alpha}/L_{\text{FUV}})(\text{observed})$  vs.  $A_{\text{H}\alpha}$  should equal  $0.4(A_{\text{FUV}}/A_{\text{H}\alpha} - 1)$ .

Note that the SFR matching method assumes that the SFR is approximately constant over a timescale of  $\sim 100$  Myrs.  $\text{H}\alpha$  is most sensitive to star formation on a timescale of about 10 Myrs, since only the most luminous stars produce large quantities of hydrogen-ionizing UV flux. In contrast, the FUV is dominated by light from somewhat lower mass stars, so measures star formation over a timescale of  $\sim 100$  Myrs, and NUV even longer timescales, to  $\sim 200$  Myrs (Kennicutt & Evans 2012). Thus variations in the SFR over short timescales, such as recent bursts, can significantly affect results from the SFR matching method. This point is discussed further below.

In Figure 14, we plot the observed  $\log(L_{\text{H}\alpha}/L_{\text{FUV}})$  vs.  $A_{\text{H}\alpha}$  (bottom panels). Figure 14 also provides plots of the observed  $\log(L_{\text{H}\alpha}/L_{\text{NUV}})$  vs.  $A_{\text{H}\alpha}$  (top panels). The 1.0 kpc radius clumps are displayed in the left panels of Figure 14, while the 2.5 kpc clumps are in the right panels. The open black squares are the disk clumps in the interacting galaxies, the magenta open diamonds are the tidal clumps, and the small blue filled triangles are clumps in the disks of the spirals. Regions with SFRs greater than  $0.4 \text{ M}_{\odot} \text{ yr}^{-1}$  have a green circle around them.

On Figure 14, we overlay the standard Calzetti (2001) starburst attenuation law (red dashed curve), assuming that the FUV and NUV attenuations also obey the relations relative to 24  $\mu\text{m}$  implied by the formulae for  $\text{SFR}_{\text{FUV}+24}$  and  $\text{SFR}_{\text{NUV}+24}$  given above, i.e.,  $A_{\text{FUV}} = 2.5\log(1 + 6.0L_{24}/L_{\text{FUV}})$  (Leroy et al. 2008; Liu et al. 2011) and  $A_{\text{NUV}} = 2.5\log(1 + 2.26L_{24}/L_{\text{NUV}})$

(Hao et al. 2011). The Calzetti (2001) starburst law gives  $A_{FUV} = 1.82 A_{H\alpha}$  and  $A_{NUV} = 1.52 A_{H\alpha}$  (see Hao et al. 2011 and Boquien et al. 2015). Hao et al. (2011) found a similar  $A_{FUV}/A_{H\alpha}$  of  $2.06 \pm 0.28$  from the global fluxes of nearby star forming galaxies.

There is a large amount of scatter in the data plotted in Figure 14, without strong overall trends. However, there are differences between the high SFR regions and the rest of the clumps. In these plots, the high SFR clumps generally follow paths that trend upwards, and the data points tend to lie near or along the Calzetti relation. In contrast, the lower SFR regions show a slight trend downwards. A downward slope in these plots means that as the overall attenuation increases, the attenuation in  $H\alpha$  increases faster than that in the NUV.

We thus conclude that the Calzetti attenuation law is a reasonable match to the data for the high SFR clumps. In contrast, the downward trends for the lower luminosity regions imply smaller  $A_{FUV}/A_{H\alpha}$  and  $A_{NUV}/A_{H\alpha}$  ratios than the Calzetti law, if the SFR matching method is appropriate for those clumps.

As noted above, the SFR matching method requires an approximately constant SFR over timescales of 10 – 100 Myrs. For the highest SFR clumps in our sample, we have conducted detailed stellar population synthesis studies, and found that the broadband optical/UV/IR colors and the  $H\alpha$  data are inconsistent with a single instantaneous burst (Smith et al. 2014). Instead, population synthesis suggests that either these regions have undergone two or more bursts, or the star formation in these regions has been prolonged over an extended time period. The presence of large quantities of diffuse X-ray-emitting gas in these extreme regions (Smith et al. 2014) supports this scenario. Thus, at least for the highest luminosity regions in our sample, an assumption of a constant SFR over  $\sim 100$  Myrs may be a reasonable first approximation in estimating the dust attenuation laws. This supports the idea that the Calzetti law is appropriate for these high luminosity regions.

The Calzetti law was derived for global fluxes from starburst galaxies, and can be explained by a clumpy foreground dust screen (Calzetti et al. 1996; Calzetti 1997; Charlot & Fall 2000; Fishera, Dopita, & Smith 2003). Such a geometry gives a flatter attenua-

tion curve with wavelength (more ‘gray’) and a larger ratio of total to selective extinction than a uniform dust screen (Natta & Panagia 1984; Witt & Gordon 2000).

We conclude that our highest luminosity clumps are starburst-like in their dust attenuation. This suggests that they are also starburst-like in their dust distributions, meaning they are surrounded by clumpy dusty gas shells. Perhaps in these regions star formation is occurring inside-out, with a dense shell of gas and dust around a compact group of highly obscured hot young stars. Perhaps large quantities of gas and dust are inflowing into these regions, contributing to dust attenuation, but not yet involved in the star formation itself.

In starbursts, the ionized gas (i.e., the  $H\alpha$ ) has been found to be proportionally more attenuated than the stars (i.e., the FUV and NUV), likely because the ionized gas is more deeply embedded within dusty interstellar clouds than the overall stellar population (Calzetti, Kinney, & Storchi-Bergmann 1994; Calzetti 2001). The differential attenuation of the stars relative to the ionized gas in starburst galaxies has been found to be about a factor of 0.44 (Calzetti, Kinney, & Storchi-Bergmann 1994; Calzetti 2001).

If SFR matching holds in these regions, our results imply higher  $A_{FUV}/A_{H\alpha}$  ratios for higher SFRs. A similar conclusion was reached by Boquien et al. (2015) from a high resolution study of the nearby spiral galaxy M33. For the highest SFR regions ( $\Sigma_{SFR} \geq 0.1 M_{\odot} \text{ yr}^{-1} \text{ kpc}^{-2}$ ) at the highest spatial scale (33 pc), Boquien et al. (2015) find  $A_{FUV}/A_{H\alpha} = 3.94$ , considerably higher than the Calzetti value. Boquien et al. (2015) interpret this increase as being due to less differential attenuation of the stars and gas on that spatial scale within intense star forming regions. On that scale, the stars emitting the FUV light are more likely to be associated with the star formation and are therefore more mixed with the ionized gas and so attenuated by a similar amount of dust. In general, on small spatial scales within M33, Boquien et al. (2015) find a trend in that regions with higher SFR have larger  $A_{FUV}/A_{H\alpha}$ , suggesting less differential extinction between the stars and the gas.

In contrast to the high SFR regions, the lower luminosity clumps in our sample have increasingly smaller  $L_{H\alpha}/L_{UV}$  ratios for increasing  $H\alpha$



attenuation (Figure 14), implying that as the dust attenuation increases the attenuation in the  $H\alpha$  increases at a faster rate than that in the UV. This trend is consistent with what is found on a global scale in star forming galaxies by Wild et al. (2011); as the stellar-mass-normalized star formation rate drops, the differential attenuation between the stars and the gas increases. In other words, at lower SFRs, the fraction of the UV-emitting stars still embedded in the interstellar cloud decreases.

In general, if the UV-emitting stars are more mixed with the ionized gas, with the attenuating dust outside of the bulk of these stars, the effective  $A_{FUV}/A_{H\alpha}$  and  $A_{NUV}/A_{H\alpha}$  ratios increase, while systems with more differential attenuation between the stars and the ionized gas have lower ratios. Thus one possible explanation for our results for the low luminosity regions is that there is more differential extinction between the UV-emitting stars and the ionized gas in our clumps than in the Calzetti starburst relationship. In general, a clump in which the stars are more extended than a central concentration of interstellar gas will produce a ‘flatter’ attenuation curve (i.e., a lower  $A_{FUV}/A_{H\alpha}$  ratio) (Witt & Gordon 2000).

Alternatively, the lower apparent  $A_{FUV}/A_{H\alpha}$  ratios for the lower SFR clumps may be due to non-constant SFRs in the clumps. As noted above, by using the SFR matching technique we are implicitly assuming that the SFR is constant over the timescale that these tracers are sensitive to star formation (100 Myrs). This is a reasonable assumption for a galaxy as a whole, but less valid for an individual knot of star formation. If instead there was an instantaneous burst of star formation in the knot, then the  $H\alpha$  will fade first (with a timescale of about 10 Myrs), then the FUV, then the NUV. Instead of stronger attenuation in the  $H\alpha$  compared to the FUV, the low  $L_{H\alpha}/L_{FUV}$  ratios may be due to an aged stellar population in which the intrinsic  $L_{H\alpha}/L_{FUV}$  has dropped. In a detailed study of the star forming regions in M51, Calzetti et al. (2005) reached similar conclusions: either the dust attenuation law in the lower luminosity regions is different from that of starbursts, or older ages are affecting the UV colors and UV/IR ratios.

Another factor that can strongly affect the  $A_{FUV}/A_{H\alpha}$  ratios is the inclination of the disk.

Based on detailed population synthesis modeling and radiative transfer calculations, Wild et al. (2011) found that disk galaxies more inclined to our line of sight have larger differential attenuation between the stars and the ionized gas; in the most extreme cases the attenuation of the ionized gas can be more than four times that of the stars. In interacting galaxies, tidal distortions may exacerbate the problem, placing unrelated tidal features in front of other knots of star formation.

Other factors that may affect the observed  $L_{H\alpha}/L_{FUV}$  ratios are the metallicities, the amount and density of the gas, and the amount of  $H\alpha$  leakage out of the region. These possibilities could be tested with follow-up optical and UV spectroscopy and detailed population synthesis.

### 6.3. The Schmidt-Kennicutt Law

As noted earlier, the observed correlations between SFR and dust attenuation (Figures 10 – 12) may exist because regions with higher gas column densities have higher dust column densities, and the SFR is related to the gas column density via the Schmidt-Kennicutt Law. Globally, the disk-averaged relationship is  $\Sigma_{SFR} \propto \Sigma_{gas}^{1.4 \pm 0.15}$  (Kennicutt 1989). Spatially-resolved studies find similar relations within galaxies, with the power law index varying somewhat depending upon the galaxy and spatial scale studied (Kennicutt et al. 2007; Liu et al. 2011).

Unfortunately, high spatial resolution maps of tracers of the interstellar molecular gas (such as 2.6 mm CO emission) are not available for most of the galaxies in our sample. This means that we cannot study the Schmidt-Kennicutt Law directly in our systems. However, we can investigate it indirectly, via its effect on the dust attenuation. In external galaxies, the relationship between the dust attenuation and the gas column density in star forming regions is complicated, depending upon the geometry of the region, the metallicity, the properties of the dust, and the gas column density itself.

As an empirical method of determining the relationship between the dust attenuation and the hydrogen column density within galaxies, we use the table of spatially-resolved measurements of the  $H\alpha$  flux, the 24  $\mu\text{m}$  flux density, and total hydrogen ( $\text{HI} + \text{H}_2$ ) gas column density  $N_H$  in

500 pc diameter regions within M51 provided by Kennicutt et al. (2007). In Figure 15, we display their data in a plot of  $\log L_{H\alpha}/L_{24}$  vs.  $N_H$ . A correlation is seen. A linear fit (cyan line) gives  $\log L_{H\alpha}/L_{24} = (-0.34 \pm 0.05)(\log N_H) + (5.5 \pm 1.0)$ .

We combine this equation with the spatially-resolved Schmidt-Kennicutt law  $\Sigma_{SFR}$  (in  $M_\odot \text{ yr}^{-1} \text{ kpc}^{-2}$ )  $= 4.8 \times 10^{-5} \Sigma_{gas}^{1.56}$  derived by Kennicutt et al. (2007) for 500 pc diameter regions within M51. The resultant relationship is overplotted on our  $L_{H\alpha}/L_{24}$  vs. SFR plots in Figure 16 as cyan dashed lines. We see good agreement between these curves and our best-fit lines, implying that the Schmidt-Kennicutt law holds in our regions.

To investigate this issue further, we utilize the relationship between FUV extinction and hydrogen column density derived by Boquien et al. (2013) from a multi-wavelength spatially-resolved study of a sample of four very nearby spiral galaxies at a resolution of  $0.5 - 2.5$  kpc. Using broadband UV/optical/IR population synthesis, they determined the FUV optical depth within these galaxies, and compared to tracers of the interstellar gas. Assuming a slab geometry (i.e., a uniformly mixed distribution of stars and dust), they derive the relationship  $\tau_{FUV} = (2.226 \pm 0.040) + (0.058 \pm 0.001) \times \Sigma_H$ , where  $\Sigma_H$  is in  $M_\odot \text{ pc}^{-2}$ . We combine this relationship with the spatially-resolved Schmidt-Kennicutt law, and plot it on our FUV - [24] vs. SFR plot in Figure 17 (magenta dotted curve) along with our best linear fit to the data (blue solid curve). The combination of the Boquien et al. (2013) attenuation model and the Schmidt-Kennicutt law provides a fairly good match to our data.

At the high SFR end of the plots in Figures 16 and 17, the datapoints appear to have higher attenuations at  $H\alpha$  and FUV than expected based on a linear fit (blue solid line), the M51-derived expectation (Figure 16; dashed cyan curves), or the Boquien et al. (2013) relation (Figure 17; dotted magenta curves). In other words, for the highest SFR clumps the SFRs are lower than expected based on these relationships. There has been some discussion recently in the literature suggesting that the Schmidt-Kennicutt law in starburst galaxies may differ from that in spirals (Daddi et al. 2010; Boquien et al. 2011), with significantly higher SFRs per gas surface density in the starbursts (i.e., a ‘starburst mode’ with higher

star formation efficiencies). In our highest SFR clumps, however, the SFR per dust attenuation is lower than expected based on the correlations seen at lower SFRs. This is the opposite of what is expected if the efficiency of star formation is higher in these regions, unless the dust attenuation to gas column density relation also differs in these regions. If large quantities of gas are flowing into these regions but are not yet engaged in star formation, the attenuation may be high relative to the SFR. High spatial resolution CO observations of some of these high SFR regions, particularly the hinge clumps in Arp 240 and Arp 256, would be useful in testing this scenario by determining the  $\Sigma_{SFR} - N_H$  relation directly in these regions.

## 7. Summary

We extracted fluxes for clumps of star formation within 46 pre-merger interacting galaxies and 39 isolated spirals. We find a flatter distribution of SFRs for the clumps in the interacting galaxies (i.e., proportionally more clumps at higher luminosities) than those in the spirals. If our tracers of SFR are consistent from region to region and are unbiased, this implies that there are more young stars, on average, per region in the interacting galaxies (i.e., a higher density of stars). This means that either the efficiency of star formation per region is higher in interacting galaxies, or there is more interstellar gas per clump, or both. On average, a larger fraction of the total flux of the interacting galaxies is contained in the clumps, compared to the spirals.

With the exception of the overlap region in the Antennae, the highest SFR clumps in our sample are located near the base of tidal features in interacting galaxies. Strong star formation may be triggered in these regions by converging gas flows along narrow caustics (Struck & Smith 2012). Published HST images reveal unusually large and luminous star clusters at the heart of the most luminous clumps in our sample (Smith et al. 2014).

For the highest SFR regions, the implied  $H\alpha$ -to-UV dust attenuation is consistent with the Calzetti starburst law, assuming an approximately constant SFR over  $\sim 100$  Myrs. This suggests that the young stars in these regions are surrounded by a clumpy dusty shell of gas, with moderate

star/ionized gas differential dust attenuation. For the lower luminosity clumps, either the SFR has faded in the last  $\sim 10 - 50$  Myrs or there is enhanced differential attenuation between the FUV-emitting stars and the ionized gas.

The inferred dust attenuation of our clumps increases with increasing SFR. This is consistent with the Schmidt-Kennicutt relation between SFR and gas surface density, with regions with higher gas content having higher SFRs. We do not see evidence for a ‘starburst’ mode of star formation (i.e., high star formation efficiency) in our highest SFR clumps, if the dust attenuation to gas column density relations for these regions are similar to those of the other clumps in the sample.

This research was supported by National Science Foundation Extragalactic Astronomy grant AST-1311935. We thank the anonymous referee for very helpful comments that greatly improved this paper. We also thank Joan Font and Artemi Camps-Fariña for help with the WHT observations. We also acknowledge Mark Giroux and Brad Peterson for helpful comments, and Ashton Morelock for help with downloading and checking data. This research has made use of the NASA/IPAC Extragalactic Database (NED), which is operated by the Jet Propulsion Laboratory, California Institute of Technology, under contract with NASA. This work is based in part on observations made with the Spitzer Space Telescope, which is operated by the Jet Propulsion Laboratory (JPL), California Institute of Technology under a contract with NASA. This study also uses data from the NASA Galaxy Evolution Explorer (GALEX), which was operated for NASA by the California Institute of Technology under NASA contract NAS5-98034. The William Herschel 4.2m Telescope is operated on the island of La Palma by the Isaac Newton Group in the Spanish Observatorio del Roque de los Muchachos of the Instituto de Astrofísica de Canarias.

## Appendix: Using Spitzer Colors to Identify Interlopers

In the absence of optical spectra or detections in  $H\alpha$  maps, a useful way of determining whether  $8\ \mu\text{m}$ -selected sources are foreground stars, background quasars, or star forming regions is to use the Spitzer broadband colors. The Spitzer  $[3.6\ \mu\text{m}] - [4.5\ \mu\text{m}]$  vs.  $[3.6\ \mu\text{m}] - [8.0\ \mu\text{m}]$  color-color diagram is especially useful for this task (Smith et al. 2005; Lapham, Smith, & Struck 2013). This color-color plot is a particularly useful diagnostic for our study, since all of the galaxies in our sample have images in these Spitzer bands. The global  $3.6\ \mu\text{m}$  emission from galaxies is generally assumed to be dominated by light from the older stellar population/underlying stellar mass while interstellar contributions dominate at wavelengths of  $5.8\ \mu\text{m}$  and longer (e.g., Helou et al. 2004). In the  $3.6\ \mu\text{m} - 8.0\ \mu\text{m}$  wavelength range, stars have spectral energy distributions (SEDs) that drop with wavelength, giving  $[3.6] - [4.5]$  and  $[3.6] - [8.0]$  colors close to zero (e.g., Whitney et al. 2004). In contrast, star forming regions have SEDs that drop from  $3.6\ \mu\text{m}$  to  $4.5\ \mu\text{m}$ , and then increase at longer wavelengths (Smith et al. 2005, 2008, 2014; Lapham, Smith, & Struck 2013; Higdon et al. 2014). Quasars typically have flat SEDs in this wavelength range, giving them redder  $[3.6] - [4.5]$  colors than both stars and most star forming regions (Hatziminaoglou et al. 2005; Smith et al. 2005).

In Figures 18 and 19, we display  $[3.6] - [4.5]$  vs.  $[3.6] - [8.0]$  color-color plots for our 1.0 kpc clump sample, with the clumps color-coded according to their classification. Figure 18 plots the colors of the clumps in and near the interacting galaxies, while Figure 19 gives the clumps for the spirals. The corresponding plots for the 2.5 kpc radii clumps are similar and thus not shown. The left panels of Figures 18 and 19 show the disk clumps (black open squares for the interacting galaxies and filled blue triangles for the spirals) and the tidal clumps in the interacting galaxies (magenta open diamonds). The right panels of Figures 18 and 19 give the location of the nuclei (red open diamonds) and ‘off’ clumps (small green open squares). For comparison, in Figures 18 and 19 we also include Spitzer colors for H II regions in the Small and Large Magellanic Clouds from Lawton et al. (2010), with the blue crosses being regions in the LMC and the cyan plus signs being SMC regions. In Figures 18 and 19, we mark the expected location of stars by blue dotted lines (Whitney et al. 2004), and that of quasars by black dashed lines (Hatziminaoglou et al. 2005). Note that many of the objects classified as ‘off’ sources lie in these marked areas, along with a few of the galactic nuclei. Proportionally, only a few of the clumps classified as ‘disk’ or ‘tidal’ are found in these areas.

Note that for the disk clumps in both the interacting sample and the spiral galaxies, there is a trend such that the regions with the reddest  $[3.6] - [8.0]$  colors are also somewhat redder on average in  $[3.6] - [4.5]$  (see left panels in Figures 18 and 19). This is likely due to interstellar contributions at  $4.5\ \mu\text{m}$  (e.g., Lapham, Smith, & Struck 2013; Smith et al. 2014). For spiral galaxies as a whole, both the  $3.6\ \mu\text{m}$  and  $4.5\ \mu\text{m}$  Spitzer bands are generally assumed to be dominated by starlight, as the global  $[3.6] - [4.5]$  colors of spirals are usually close to zero (within 0.1 magnitudes) (e.g., Pahre et al. 2004; Smith et al. 2007). However, within interacting galaxies localized knots of intense star formation sometimes have large excesses above the stellar continuum in the  $3.6\ \mu\text{m}$  and  $4.5\ \mu\text{m}$  bands, particularly in the  $4.5\ \mu\text{m}$  filter (Smith et al. 2008; Zhang, Gao, & Kong 2010; Boquien et al. 2010).

In Figures 18 and 19, the SMC regions are redder in  $[3.6] - [4.5]$  for the same  $[3.6] - [8.0]$  color compared to the regions within the interacting galaxies. This may be a consequence of lower metallicity. Such an offset is also seen in the global colors of low metallicity dwarfs compared to higher metallicity galaxies (Smith & Hancock 2009).

Some of our ‘off’ sources are found in the same part of the color-color diagram as the ‘disk’ and ‘tail’ sources. The nature of these sources is uncertain. They may be either star forming regions in the outskirts of our target galaxies, outside of our isophote limits, or they may be background galaxies. Some of the ‘off’ sources lie in the same section of the color-color diagram as the SMC regions, as do some of the clumps classified as ‘disk’ and ‘tidal’. If they were not detected in  $H\alpha$ , the identification of these sources is ambiguous; they could be either low metallicity star forming regions in the outskirts of the target galaxy or background objects.

## REFERENCES

- Adamo, A., Kruijssen, J. M. D., Bastian, N., Silva-Villa, E., & Ryon, J. 2015, *MNRAS*, 452, 246
- Adamo, A., Östlin, G., & Zackrisson, E. 2011, *MNRAS*, 417, 1904
- Armus, L., Heckman, T., & Miley, G. 1987, *AJ*, 94, 831
- Arp, H. 1966, *Atlas of Peculiar Galaxies* (Pasadena: Caltech)
- Barnes, J. E. & Hernquist, L. E. 1991, *ApJ*, 370, L65
- Barton, E. J., Geller, M. J., & Kenyon, S. J. 2000, *ApJ*, 530, 660
- Barton Gillespie, E., Geller, M. J., & Kenyon, S. J. 2003, *ApJ*, 582, 668
- Benn, C., Dee, K., & Agócs, T. 2008, *SPIE*, 7014, 6
- Beirão, P., Appleton, P. N., Brandl, B. R., Seibert, M., Jarrett, T., & Houck, J. R. 2009, *ApJ*, 693, 1650
- Boquien, M., Boselli, A., Buat, V., et al. 2013, *A&A*, 554, A14
- Boquien, M., Buat, V., Boselli, A., et al. 2012, *A&A*, 539, 145
- Boquien, M., Calzetti, D., Aalto, S., et al. 2015, *A&A*, 578, 8
- Boquien, M., Calzetti, D., Kennicutt, R., et al. 2009, *ApJ*, 706, 553
- Boquien, M., Duc, P.-A., Braine, J., Brinks, E., Lisenfeld, U., & Charmandaris, V. 2007, *A&A*, 467, 93
- Boquien, M., Duc, P.-A., Galliano, F., Braine, J., Lisenfeld, U., Charmandaris, V., & Appleton, P. N. 2010, *AJ*, 140, 2124
- Boquien, M., Duc, P.-A., Wu, Y., Charmandaris, V., Lisenfeld, U., Braine, J., Brinks, E., Iglesias-Páramo, J., & Xu, C. K. 2009, *AJ*, 137, 4561
- Boquien, M., Lisenfeld, U., Duc, P.-A., Braine, P., Bournaud, F., Brinks, E., & Charmandaris, V. 2011, *A&A*, 533, A19
- Boselli, A., Lequeux, J., Sauvage, M., et al. 1998, *A&A*, 335, 53
- Bournaud, F., Chapon, D., Teyssier, R., et al. 2011, *ApJ*, 730, 4
- Bournaud, F., Duc, P.-A., & Emsellem, E. 2008, *MNRAS*, 389, L8
- Buat, V., Boselli, A., Gavazzi, G., & Bonfanti, C. 2002, *A&A*, 383, 801.
- Buat, V. & Burgarella, D. 1998, *A&A*, 334, 772
- Buat, V., Donas, J., Milliard, B., & Xu, C. 1999, *A&A*, 352, 371
- Burgarella, B., Buat, V., Iglesias-Páramo, J. 2005, *MNRAS*, 360, 1413
- Bushouse, H. A. 1987, *ApJ*, 320, 49
- Bushouse, H. A., Lamb, S. A., & Werner, M. W. 1988, *ApJ*, 335, 74
- Calzetti, D. 1997, *AJ*, 113, 162
- Calzetti, D. 2001, *PASP*, 113, 1449
- Calzetti, D., Kinney, A. L., & Storchi-Bergmann, T. 1994, *ApJ*, 429, 582
- Calzetti, D., Kinney, A. L., & Sorchi-Bergmann, T. 1996, *ApJ*, 458, 132
- Calzetti, D., Kennicutt, R. C., Jr., Bianchi, L., et al. 2005, *ApJ*, 633, 871
- Calzetti, D., Kennicutt, R. C., Engelbracht, C. W., et al. 2007, *ApJ*, 666, 870
- Cao, C. & Wu, H. 2007, *AJ*, 133, 1710
- Cardelli, J. A., Clayton, G. L., & Mathis, J. S. 1989, *ApJ*, 345, 245
- Clements, D. L. & Baker, A. C. 1996, *A&A*, 314, L5
- Clements, D. L., Sutherland, W. J., McMahon, R. G., & Saunders, W. 1996, *MNRAS*, 279, 477
- Conroy, C., Schiminovich, D., and Blanton, M. R. 2010, *ApJ*, 718, 184

- Charlot, S. & Fall, S. M. 2000, *ApJ*, 539, 718
- Daddi, E., Elbaz, D., Walter, F., et al. 2010, *ApJ*, 714, L118
- Dale, D. A., Cohen, S. A., Johnson, L. C., et al. 2009, *ApJ*, 703, 517
- de Vaucouleurs, G., de Vaucouleurs, A., Corwin, Jr., H. G., Buta, R. J., Paturel, G., & Pogue, P. 1991, *Third Reference Catalogue of Bright Galaxies, Version 3.9* (Springer: New York, NY)
- Di Matteo, P., Combes, F., Melchior, A.-L., & Semelin, B. 2007, *A&A*, 468, 61
- Dors, O. L., Jr., Storchi-Bergmann, T., Riffel, R. A., & Schimdt, A. A. 2008, *A&A*, 482, 59
- Duc, P.-A., Bournaud, F., & Masset, F. 2004, *A&A*, 427, 803
- Duc, P.-A., Brinks, E., Winks, J. E., & Mirabel, I. F. 1997, *A&A*, 326, 537
- Duc, P.-A., & Mirabel, I. 1994, *A&A*, 289, 83
- Duc, P.-A., Brinks, E., Springel, V. et al. 2000, *AJ*, 120, 1238
- Ellison, S. L., Patton, D. R., Simard, L., & McConnell, A. W. 2008, *AJ*, 135, 1877
- Elmegreen, B. G., 2008, *ApJ*, 672, 1006
- Elmegreen, B. G. & Efremov, Y. N. 1996, *ApJ*, 466, 802
- Elmegreen, B. G., Kaufman, M., & Thomasson, M. 1993, *ApJ*, 412, 90
- Elmegreen, D. M., Kaufman, M., Brinks, E., Elmegreen, B. G., & Sundin, M. 1995, *ApJ*, 453, 100
- Elmegreen, D. M., Elmegreen, B. G., Kaufman, M., Sheth, K., Struck, C., Thomasson, M., & Brinks, E. 2006, *ApJ*, 642, 158
- Elmegreen, D. M., Elmegreen, B. G., Marcus, M. T., Shahinyan, K., Yau, A., & Petersen, M. 2009, *ApJ*, 701, 306
- Elmegreen, D. M., Kaufman, M., Elmegreen, B. G., & Brinks, E., Struck, C., Klaric, M., & Thomasson, M. 2001, *AJ*, 121, 182
- Engelbracht, C. W., Gordon, K. D., Rieke, G. H., Werner, M. W., Dale, D. A., & Latter, W. B. 2005, *ApJ*, 628, 29
- Epinat, B., Amram, P., & Marcelin, M. 2008, *MNRAS*, 390, 466
- Fazio, G. G., Hora, J. L., Allen, L. E., et al. 2004, *ApJS*, 154, 10
- Fellhauer, M. & Kroupa, P. 2005, *MNRAS*, 359, 223
- Fishera, J., Dopita, M. A., & Sutherland, R. S. 2003, *ApJ*, 599, L21
- Förster Schreiber, N. M., Shapley, A. E., Genzel, R., et al. 2011, *ApJ*, 739, 45
- Freedman Woods, D., Geller, M. J., Kurtz, M. J., Westra, E., Fabricant, D. G., & Dell’Antonio, I. 2010, *AJ*, 139, 1857
- García-Barreto, J. & Antonio, R. M. 2001, *AJ*, 121, 2540
- Genzel, R., Tacconi, L. J., Gracia-Carpio, J., et al. 2010, *MNRAS*, 407, 2091
- Gieles, M. 2010, in *Proceedings of the ‘Galaxy Wars: Stellar Populations and Star Formation in Interacting Galaxies’ Conference*, eds. B. Smith, N. Bastian, S. J. U. Higdon, and J. L. Higdon, *ASP Conf. Proc.* 423, 123
- Gil de Paz, A., Boisser, S., Madore, B. F., et al. 2007, *ApJS*, 173, 185
- Goddard, Q. E., Bastian, N., & Kennicutt, R. C. 2010, *MNRAS*, 405, 857
- Granato, G. L., Lacey, C. G., Silva, L., Bressan, A., Baugh, C. M., Cole, S., & Frenk, C. S. 2000, *ApJ*, 542, 710
- Gutiérrez, L., Beckman, J. E., & Buenrostro, V. 2011, *AJ*, 141, 113
- Hancock, M., Smith, B. J., Struck, C., Giroux, M. L., & Hurlock, S. 2009, *AJ*, 137, 4643
- Hancock, M., Smith, B. J., Struck, C., Giroux, M. L., Appleton, P. N., Charmandaris, V., & Reach, W. T. 2007, *AJ*, 133, 676

- Hao, C.-N., Kennicutt, R. C., Johnson, B. D., Calzetti, D., Dale, D. A., & Moustakas, J. 2011, *ApJ*, 741, 12
- Hatziminaoglou, E., Pérez-Fournon, I., Polletta, M., et al. 2005, *AJ*, 129, 1198
- Helou, G., Roussel, H., Appleton, P., et al. 2004, *ApJS*, 154, 253
- Hibbard, J. E. & van Gorkom, J. H. 1996, *AJ*, 111, 655
- Holtzman, J. A., Hester, J. J., Casertano, S., et al. 1995, *PASP*, 107, 156
- Hopkins, P. F., Quataert, E., & Murray, N. 2012, *MNRAS*, 421, 3522
- Hoopes, C. G., Walterbos, R. A. M., & Bothun, G. D. 2001, *ApJ*, 559, 878
- Howell, J. H., Armus, L., Mazzarella, J. M. et al. 2010, *ApJ*, 715, 572
- Higdon, S. J. U., Higdon, J. L., Smith, B. J., & Hancock, M. 2014, *ApJ*, 787, 103
- Hopkins, A. M., Connolly, A. J., Haarsma, D. B., & Cram, L. E. 2001, *AJ*, 122, 288
- Hunter, D. A., & Elmegreen, B. G. 2004, *AJ*, 128, 2170
- Irwin, J. A. 1994, *ApJ*, 429, 618
- Jester, S., Schneider, D. P., Richards, G. T. 2005, *AJ*, 130, 873
- Kaufman, M., Grupe, D., Elmegreen, B. G., Elmegreen, D. M., Struck, C., & Brinks, E. 2012, *AJ*, 144, 156
- Kaviraj, S., Darg, D., Lintott, C., Schawinski, K., & Silk, J. 2012, *MNRAS*, 419, 70
- Keel, W. C., Kennicutt, R. C., Jr., Hummel, E., & van der Hulst, J. M. 1985, *AJ*, 90, 708
- Kennicutt, R. C., Jr. 1984, *ApJ*, 287, 116
- Kennicutt, R. C., Jr., 1989, *ApJ*, 344, 685
- Kennicutt, R. C., Jr., 1988, *ApJ*, 334, 144
- Kennicutt, R. C., Jr., 1998, *ARA&A*, 36, 189
- Kennicutt, R. C., Armus, L., Bendo, G. et al. 2003, *PASP*, 115, 928
- Kennicutt, R. C., Jr., Keel, W. C., & Blaha, C. A. 1989, *AJ*, 97, 1022
- Kennicutt, R. C., Jr., Roettinger, K. A., Keel, W. C., van der Hulst, J. M., & Hummel, E., 1987, *AJ*, 93, 1011
- Kennicutt, R. C., Jr., Calzetti, D., Walter, F., et al. 2007, *ApJ*, 671, 333
- Kennicutt, R. C., Jr. & Chu, Y.-H. 1988, *AJ*, 95, 720
- Kennicutt, R. C., Jr., Edgar, B. K., and Hodge, P. W. 1989, *ApJ*, 337, 761
- Kennicutt, R. C., Jr. & Evans, N. J. 2012, *ARAA*, 50, 531
- Kennicutt, R. C., Jr., Hao, C.-N., Calzetti, D., et al. 2009, *ApJ*, 703, 1672
- Knapen, J. H., Stedman, S., Bramich, D. M., Folkes, S. L., & Bradley, T. R. 2004, *A&A*, 426, 1135
- Koopmann, R. A., Kenney, J. D. P., & Young, J. 2001, *ApJS*, 135, 125
- Kruijssen, J. M. D. 2012, *MNRAS*, 426, 3008
- Lambas, D. G., Tissera, P. B., Alonso, M. S., & Coldwell, G. 2003, *MNRAS*, 346, 1189
- Lapham, R. C., Smith, B. J., & Struck, C. 2013, *AJ*, 145, 130
- Larsen, S. S. 2004, *A&A*, 416, 537
- Larson, R. B. & Tinsley, B. M. 1978, *ApJ*, 219, 46
- Lawton, B., Gordon, K. D., Babler, B., et al. 2010, *ApJ*, 716, 453
- Leech, K. J., Rowan-Robinson, M., Lawrence, A., & Hughe, J. D. 1994, *MNRAS*, 267, 253
- Leroy, A. K., Walter, F., Brinks, E., et al. 2008, *AJ*, 136, 2782
- Li, A. & Draine, B. T. 2001, *ApJ*, 554, 778
- Li, C., Kaufmann, G., Heckman, T. M., Jing, Y. P., & White, S. D. M. 2008, *MNRAS*, 385, 1903

- Lin, L., Koo, D. C., Weiner, B. J., et al. 2007, *ApJ*, 660, L51
- Liu, G., Koda, J., Calzetti, D., Fukuhara, M., & Momose, R. 2011, *ApJ*, 735, 63
- Lonsdale, C. J., Persson, S. E., & Matthews, K. 1984, *ApJ*, 287, 95
- Mao, Y.-W., Kong, X., & Lin, L. 2014, *ApJ*, 789, 76
- Melnick, J. & Mirabel, I. F. 1990, *A&A*, 231, L19
- Mihos, J. C. & Hernquist, L. 1996, *ApJ*, 464, 641
- Mirabel, I. F., Lutz, D., & Maza, J. 1991, *A&A*, 243, 367
- Mirabel, I. F., Dottori, H., & Lutz, D. 1992, *A&A*, 256, L19
- Natta, A. & Panagia, N. 1984, *ApJ*, 287, 228
- Nikolic, B., Cullen, H., & Alexander, P. 2004, *MNRAS*, 355, 874
- Pahre, M. A., Ashby, M. L. N., Fazio, G. G., & Willner, S. P. 2004, *ApJS*, 154, 235
- Panuzzo, P., Granato, G. L., Buat, V., Inoue, A. K., Silva, L., Iglesias-Páramo, J., & Bressan, A. 2007, *MNRAS*, 375, 640
- Pancoast, A., Sajini, A., Lacy, M., Noriega-Crespo, A., & Rho, J. 2010, *ApJ*, 723, 530
- Peterson, B. W., Struck, C., Smith, B. J., & Hancock, M. 2009, *MNRAS*, 400, 1208
- Powell, L. C., Bournaud, F., Chapon, D., & Teyssier, R. 2013, *MNRAS*, 434, 1028
- Quillen, A. C. & Bland-Hawthorn, J. 2008, *MNRAS*, 386, 2227
- Renaud, F., Bournaud, F., Kraljic, K., & Duc, P.-A. 2014, *MNRAS*, 442, L33
- Renaud, F., Kraljic, K., & Bournaud, F. 2012, *ApJ*, 760, L16
- Rieke, G. H., Young, E. T., Engelbracht, C. W., et al. 2004, *ApJS*, 154, 25
- Rieke, G. H., Alonso-Herrero, A., Weiner, B. J., Pérez-González, P. G., Blaylock, M., Donley, J. L., & Marcillas, D. 2009, *ApJ*, 692, 556
- Rigopoulou, D., Spoon, H. W. W., Genzel, R., et al. 1999, *AJ*, 118, 2625
- Romanishin, W. 1983, *MNRAS*, 204, 909
- Rosenberg, J. L., Ashby, M. L. N., Salzer, J. J., & Huang, J.-S., 2006, *ApJ*, 636, 742
- Rosenberg, J. L., Wu, Y., Le Floch, E., Charmandaris, V., Ashby, M. L. N., Houck, J. R., Salzer, J. J., & Willner, S. P. 2008, *ApJ*, 674, 814
- Ryon, J. E., Adamo, A., Bastian, N., et al. 2014, *AJ*, 148, 33
- Saintonge, A., Tacconi, L. J., Fabello, S., et al. 2012, *ApJ*, 758, 73
- Sanders, D. B. & Mirabel, I. F. 1996, *ARA&A*, 34, 749
- Sanders, D. B., Soifer, B. T., Elias, J. H., Neugebauer, G., & Matthews, K. 1988, *ApJ*, 328, L35
- Sarzi, M., Allard, E. L., Knapen, J. H., & Mazuca, L. M. 2007, *MNRAS*, 380, 949
- Scalo, J. M. & Struck-Marcell, C. 1986, *ApJ*, 301, 77
- Schlafly, E. F. & Finkbeiner, D. P. 2011, *ApJ*, 737, 103
- Schmidt, M. 1959, *ApJ*, 129, 243
- Schweizer, F. in *Structure and Properties of Nearby Galaxies*, ed. E. M. Berkhuysen & R. Wielebinski (Dordrecht: Reidel), 279
- Silverman, J. D., Daddi, E., Rodighiero, G., et al. 2015, *ApJ*, 812, L23
- Skrutskie, M. F., Cutri, R. M., Stiening, R., et al. 2006, *AJ*, 131, 1163.
- Smith, B. J. & Hancock, M. 2009, *AJ*, 138, 130
- Smith, B. J., Kleinmann, S. G., Huchra, J. P., & Low, F. 1987, *ApJ*, 318, 161
- Smith, B. J., Struck, C., Appleton, P. N., Charmandaris, V., Reach, W. & Eitter, J. J. 2005, *AJ*, 130, 2117
- Smith, B. J., Struck, C., Hancock, M., Appleton, P. N., Charmandaris, V. & Reach, W. 2007, *AJ*, 133, 791



- Smith, B. J., Struck, C., Hancock, M., et al. 2008, *AJ*, 135, 2406
- Smith, B. J., Giroux, M. L., Struck, C., Hancock, M., and Hurlock, S. 2010, *AJ*, 139, 1212; Erratum 2010, *AJ*, 139, 2719
- Smith, B. J., Struck, C., & Nowak, M. A. 2005, *AJ*, 129, 1350
- Smith, B. J., Struck, C., & Pogge, R. W. 1997, *ApJ*, 483, 754
- Smith, B. J. & Struck, C. 2010, *AJ*, 140, 1975
- Smith, B. J., Swartz, D. A., Miller, O., Burleson, J. A., Nowak, M. A., & Struck, C. 2012, *AJ*, 143, 144
- Smith, B. J., Soria, R., Struck, C., Giroux, M. L., Swartz, D. A., & Yukita, M. 2014, *AJ*, 147, 60
- Sol Alonso, M., Lambas, D. G., Tissera, P., & Coldwell, G. 2006, *MNRAS*, 367, 1029
- Stetson, P. B. 1987, *PASP*, 99, 191
- Struck, C. & Smith, B. J. 2003, *ApJ*, 589, 157
- Struck, C. & Smith, B. J. 2012, *MNRAS*, 422, 2444
- Struck, C., Dobbs, C. L., & Hwang, J.-S. 2011, *MNRAS*, 414, 2498
- Struck, C., Kaufman, M., Brinks, E., Thomasson, M., Elmegreen, B. G., & Elmegreen, D. M. 2005, *MNRAS*, 364, 69
- Sullivan, M., Mobasher, B., Chan, B., Cram, L., Ellis, R., Treyer, M., & Hopkins, A. 2001, *ApJ*, 558, 72
- Teyssier, R., Chapon, D., & Bournaud, F. 2010, *ApJ*, 720, L149
- Torres-Flores, S., Mendes de Oliveira, C., de Mello, D. F., et al. 2009, *A&A*, 507, 723
- Treyer, M., Schiminovich, D., Johnson, B., et al. 2007, *ApJS*, 173, 256
- van den Bergh, S. 1960, *ApJ*, 131, 215
- Wang, B. & Heckman, M. 1996, *ApJ*, 457, 645
- Wetzstein, M., Naab, T., & Burkert, A. 2007, *MNRAS*, 375, 805
- Whitmore, B. C., Chandar, R., Schweizer, F., et al. 2010, *AJ*, 140, 75
- Whitney, B. A., Indebetouw, R., Babler, B. L., et al. 2004, *ApJS*, 154, 315
- Wild, V., Charlot, S., Brinchmann, J., et al. 2011, *MNRAS*, 417, 1760
- Williams, B. F., Binder, B. A., Dalcanton, J. J., Eracleous, M., & Dolphin, A. 2013, *ApJ*, 772, 12
- Witt, A. N. & Gordon, K. D. 2000, *ApJ*, 528, 799
- Woods, D. F., Geller, M. J., & Barton, E. J. 2006, *AJ*, 132, 197
- Wu, H., Cao, C., Liu, F.-S., Wang, J.-L., Xia, X.-Y., Deng, Z.-G., & Young, K. S. 2005, *ApJ*, 632, L79
- Yuan, F. T., Takeuchi, T. T., Matsuoka, Y., et al. 2012, *A&A*, 548, A117
- Zhang, H.-X., Gao, Y., & Kong, X. 2010, *MNRAS*, 401, 1839
- Zhu, Y., Wu, H., Cao, C., & Li, H.-N. 2008, *ApJ*, 686, 155
- Zaragoza-Cardiel, J., Font-Serra, J., Beckman, J. E., et al. 2013, *MNRAS*, 432, 998
- Zaragoza-Cardiel, J., Font, J., Beckman, J. E., García-Lorenzo, B., Erroz-Ferrer, S., & Gutiérrez, L. 2014, *MNRAS*, 445, 1412
- Zaragoza-Cardiel, J., Beckman, J. E., Font, J., et al. 2015, *MNRAS*, 451, 1307

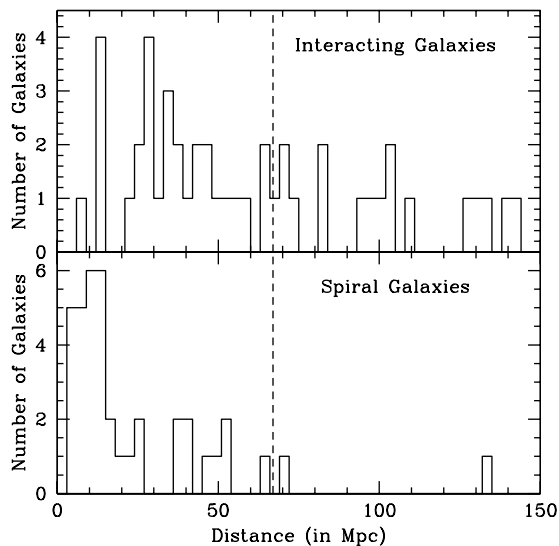


Fig. 1.— Histograms of the distances to the interacting galaxies (top panel) and the spiral galaxies (bottom panel). The dashed line at 67 Mpc shows the limit for the 1.0 kpc clump sample (see Section 4.1).

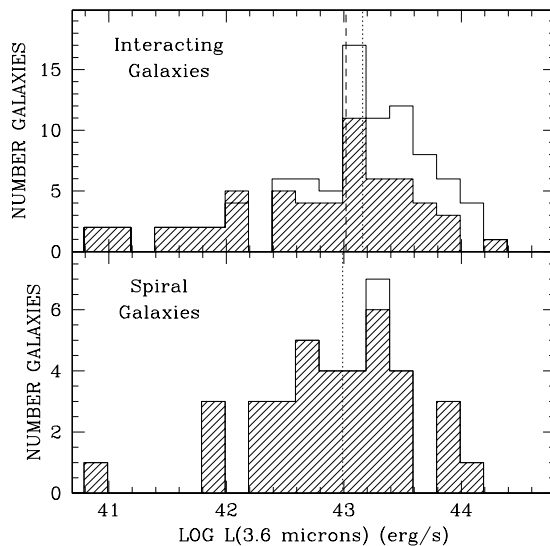


Fig. 2.— Histograms of the total 3.6  $\mu\text{m}$  luminosities ( $\nu L_\nu$ ) for the individual galaxies in the interacting galaxy pairs (top panel) and the spiral galaxies (bottom panel). The hatched histogram marks the galaxies in the 1.0 kpc clump sample (i.e., those with distances less than 67 Mpc). In the top panel, the dotted line marks the median value for the entire interacting galaxy sample ( $\log L_{3.6} = 43.16$ ), while the dashed line shows the median for the interacting galaxies with distances less than 67 Mpc ( $\log L_{3.6} = 43.02$ ). In the bottom panel, the dotted line is the median for both sets of spirals ( $\log L_{3.6} = 42.99$ ). Note that no Spitzer 3.6  $\mu\text{m}$  data is available for one of the more distant spiral galaxies, NGC 2857.

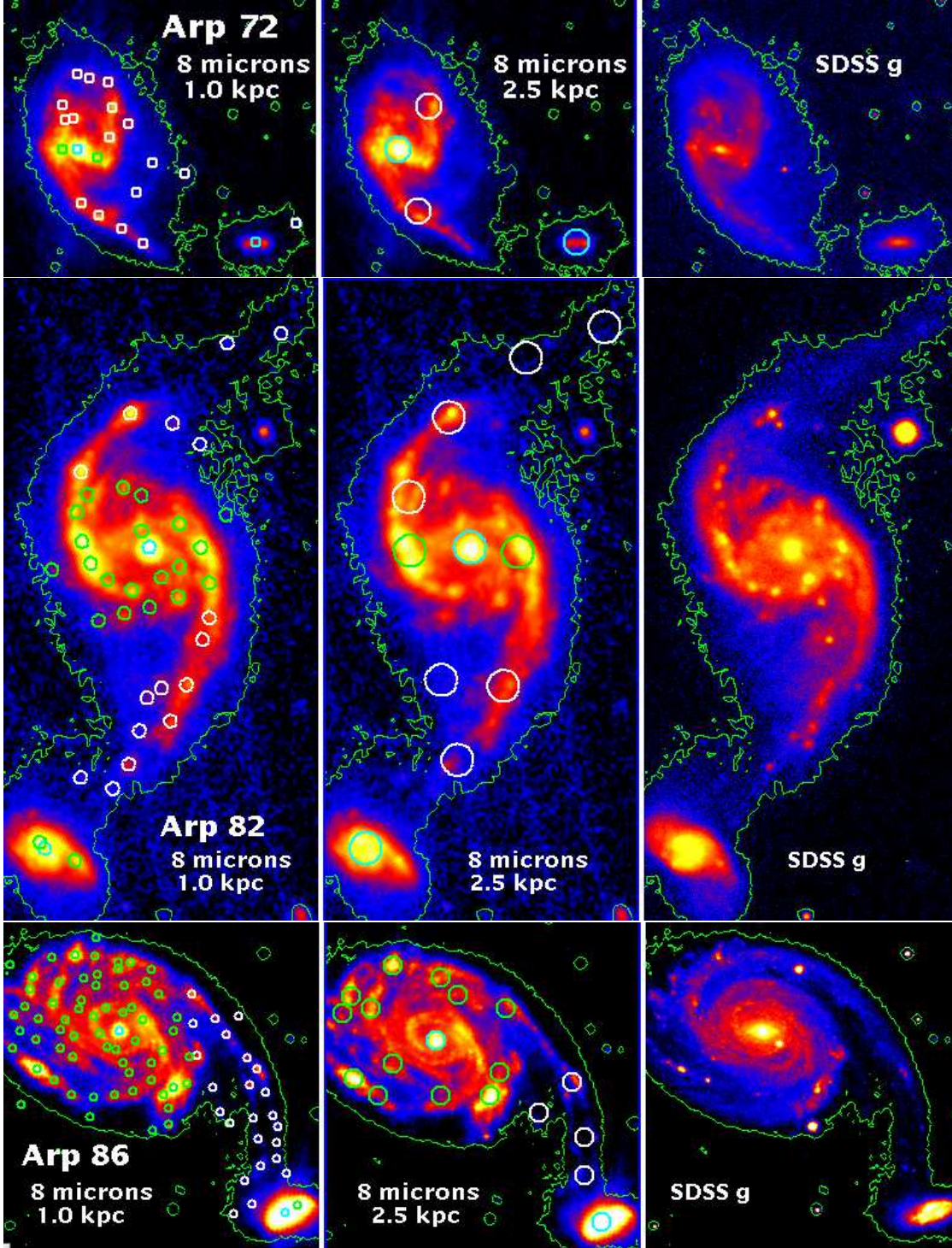


Fig. 3.— Three of the interacting galaxies in the sample, with the disk (green circles), tidal (white circles), and nuclear (cyan circles) marked. The left and middle panels display the 1.0 kpc and 2.5 kpc clump samples, respectively, superimposed on the unsmoothed Spitzer 8  $\mu$ m image. The right panels show the SDSS g image. The green contours are the SDSS g isophote of 24.58 mag/arcsec<sup>2</sup>. The top row are the images for Arp 72; the second row display the Arp 82 images, while the bottom row shows the Arp 86 images. North is up and east to the left in these pictures.

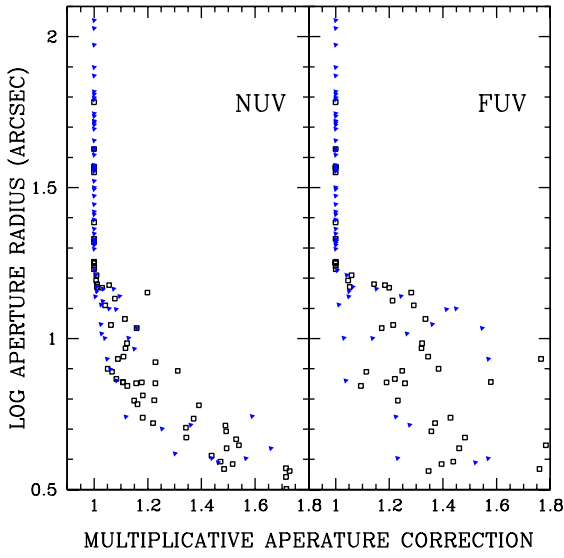


Fig. 4.— Aperture corrections for the GALEX photometry, as a function of aperture radius. The NUV values are on the left; the FUV on the right. This plot includes images from both the interacting (black open squares) and spiral (blue filled triangles) samples, and measurements for both the 1.0 kpc radius apertures and the 2.5 kpc radius apertures. See text for details.

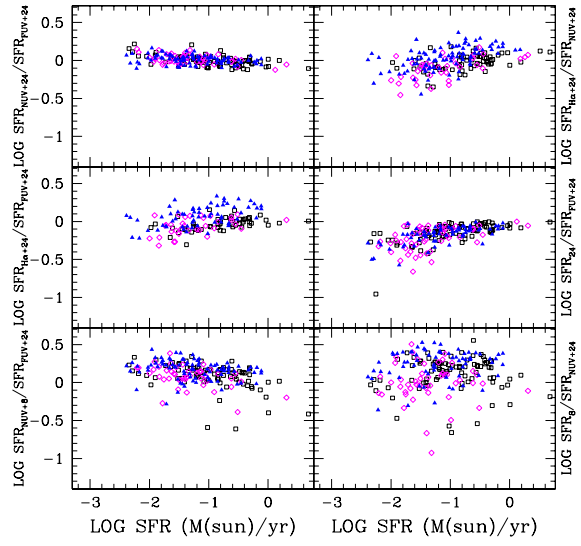


Fig. 5.— For the 2.5 kpc aperture radius clump samples, this plot provides a comparison of the SFR determined from the FUV and 24  $\mu$ m luminosities (x-axis) against various ratios of different determinations of the SFRs. Disk clumps in the interacting galaxies are shown as black open squares, clumps in the disks of the spirals are shown as blue filled triangles, and the tidal clumps in the interacting galaxies are shown as open magenta diamonds.

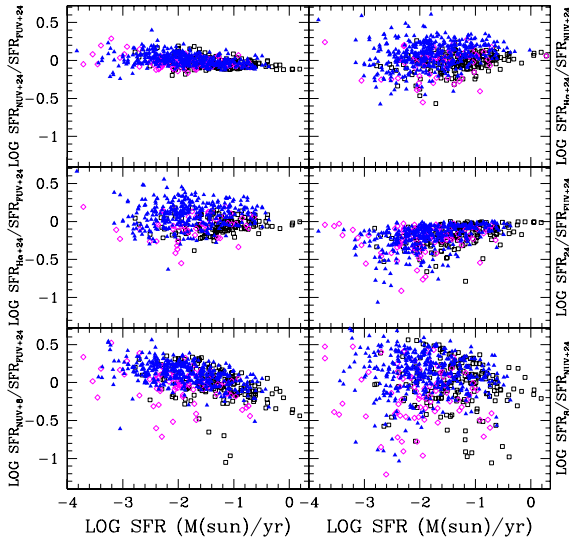


Fig. 6.— For the 1.0 kpc aperture radius clump samples, this plot provides a comparison of the SFR determined from a combination of the FUV and the  $24\ \mu\text{m}$  luminosities (x-axis) against various ratios of different determinations of the SFRs. Disk clumps in the interacting galaxies are shown as black open squares, clumps in the disks of the spirals are shown as blue filled triangles, and the tidal clumps in the interacting galaxies are shown as open magenta diamonds.

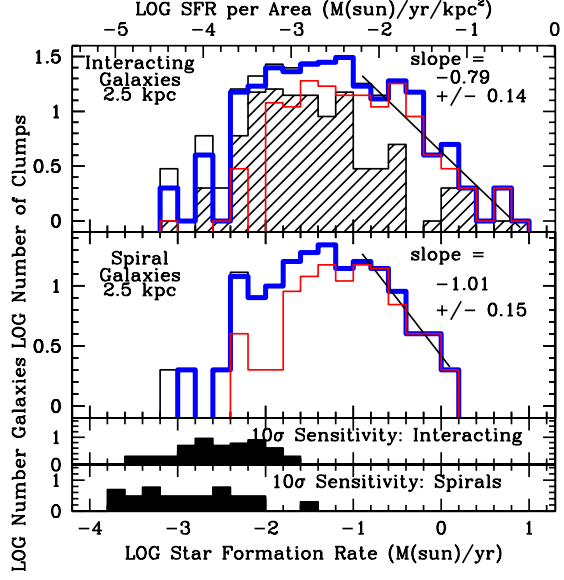


Fig. 7.— Histograms of the SFRs within the 2.5 kpc sample for the clumps in the interacting galaxies (top panel), and the disks of the normal spiral galaxies (second panel). Along the top axis of this figure, we have converted the SFRs into SFR per area, by dividing by the area per aperture. In the top panel, the tidal clumps are shown with hatch marks. The red histogram identifies clumps detected in  $\text{H}\alpha$ , while the blue includes both clumps detected in  $\text{H}\alpha$  and clumps that lie outside of the quasar and stellar regions marked in the Spitzer color-color diagrams (see Appendix). The lines are the best-fit lines to the blue histogram above  $\log \text{SFR} > -0.8$ . Histograms of the theoretical  $10\sigma$  point source sensitivities of the smoothed  $8\ \mu\text{m}$  images of the interacting and spiral galaxies are presented in the third and bottom panels, respectively. In the two bottom panels, the y-axis is the logarithm of the number of galaxies at each sensitivity.



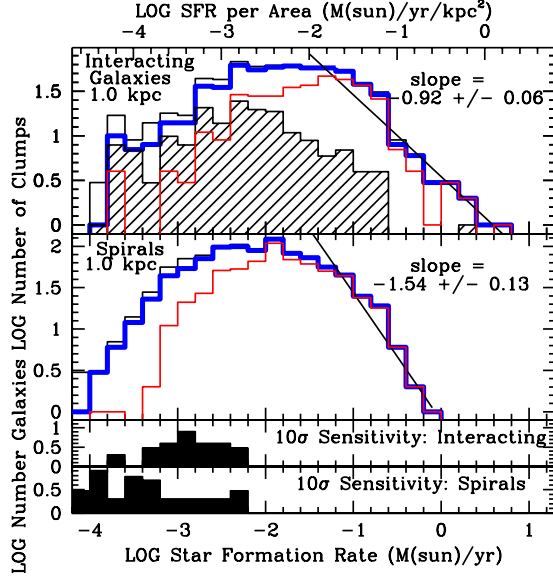


Fig. 8.— Histograms of the SFRs within the 1.0 kpc sample for the clumps in the interacting galaxies (top panel), and the disks of the normal spiral galaxies (second panel). Along the top axis of this plot, we have converted the SFRs into SFR per area, by dividing by the area per aperture. In the top panel, the tidal clumps are shown with hatch marks. The red histogram identifies clumps detected in H $\alpha$ , while the blue includes both clumps detected in H $\alpha$  and clumps that lie outside of the quasar and stellar regions marked in the Spitzer color-color diagrams (see Appendix). The lines are the best-fit lines to the blue histogram above  $\log \text{SFR} > -1.6$ . Histograms of the theoretical 10 $\sigma$  point source sensitivities of the smoothed 8  $\mu$ m images of the interacting and spiral galaxies are presented in the third and bottom panels, respectively. In the two bottom panels, the y-axis is the logarithm of the number of galaxies at each sensitivity.

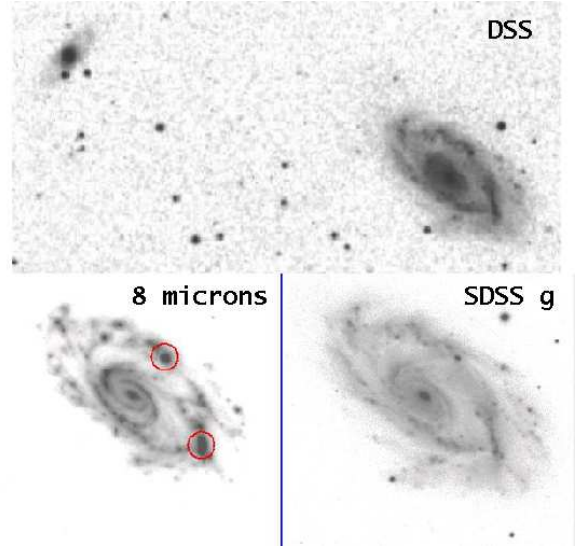


Fig. 9.— Top: the optical Digitized Sky Survey (DSS) image of NGC 3646 (larger galaxy) and its companion NGC 3649. North is up and east to the left. The field of view is  $11' \times 5'.5$ . Bottom left and right, respectively: the unsmoothed Spitzer 8  $\mu$ m and SDSS g images of NGC 3646. The field of view is  $3'.4 \times 3'.4$ . The two highest SFR clumps are circled in red in the 8  $\mu$ m image.

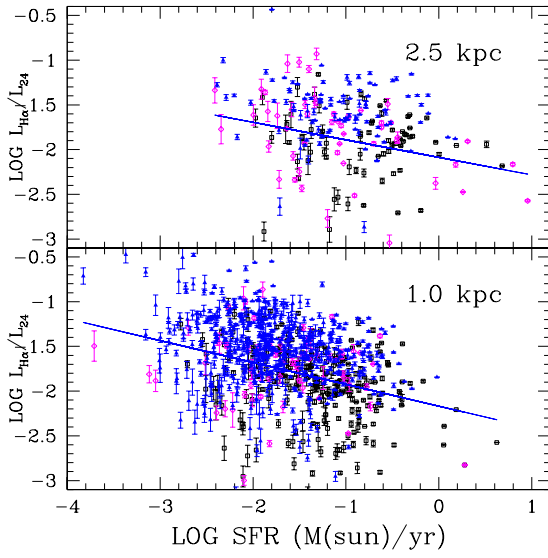


Fig. 10.— Plots of  $L_{H\alpha}/L_{24}$  vs. SFR for the 2.5 kpc clump sample (top panel) and the 1.0 kpc clump sample (bottom panel). The open black squares are the disk clumps in the interacting galaxies, while the magenta open diamonds are the tidal clumps. The small blue filled triangles mark clumps in the disks of the spirals. The solid blue line displays the best linear fit to the data.

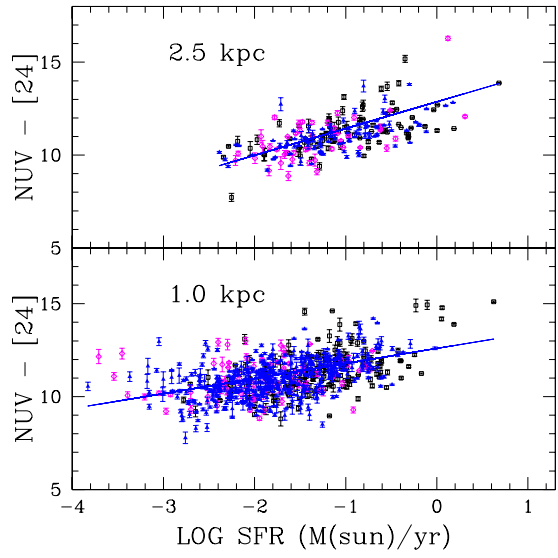


Fig. 11.— Plots of  $NUV - [24]$  vs. SFR for the 2.5 kpc clump sample (top panel) and the 1.0 kpc clump sample (bottom panel). The open black squares are the disk clumps in the interacting galaxies, while the magenta open diamonds are the tidal clumps. The small blue filled triangles mark clumps in the disks of the spirals. The solid blue line displays the best linear fit to the data.

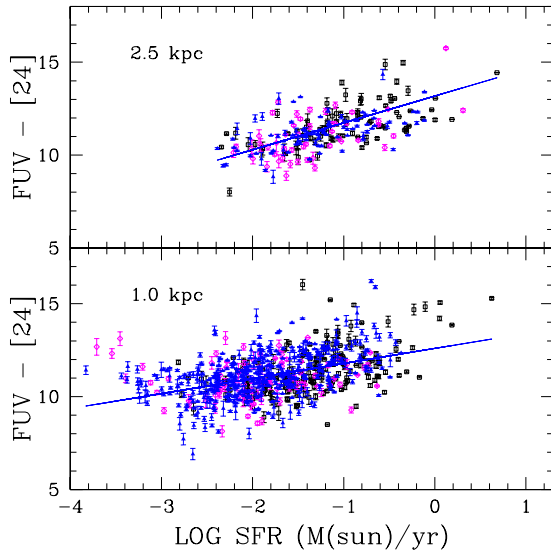


Fig. 12.— Plots of  $FUV - [24]$  vs.  $SFR$  for the 2.5 kpc clump sample (top panel) and the 1.0 kpc clump sample (bottom panel). The open black squares are the disk clumps in the interacting galaxies, while the magenta open diamonds are the tidal clumps. The small blue filled triangles mark clumps in the disks of the spirals. The solid blue line displays the best linear fit to the data.

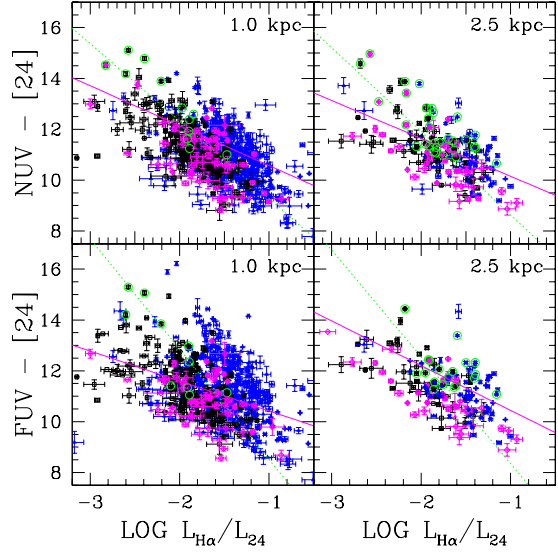


Fig. 13.— Plots of  $NUV - [24]$  vs.  $\log(L_{H\alpha}/L_{24})$  (top row) and  $FUV - [24]$  vs.  $L_{H\alpha}/L_{24}$  (bottom row) for the 2.5 kpc clump sample (right panels) and the 1.0 kpc clump sample (left panels). The open black squares are the disk clumps in the interacting galaxies, while the magenta open diamonds are the tidal clumps. The small blue filled triangles mark clumps in the disks of the spirals. The clumps circled in green have  $SFRs > 0.4 M_{\odot} \text{ yr}^{-1}$ . The magenta solid curves gives the best linear fits to all of the data, while the dotted green lines are the best fits to the clumps with  $SFRs > 0.4 M_{\odot} \text{ yr}^{-1}$ .



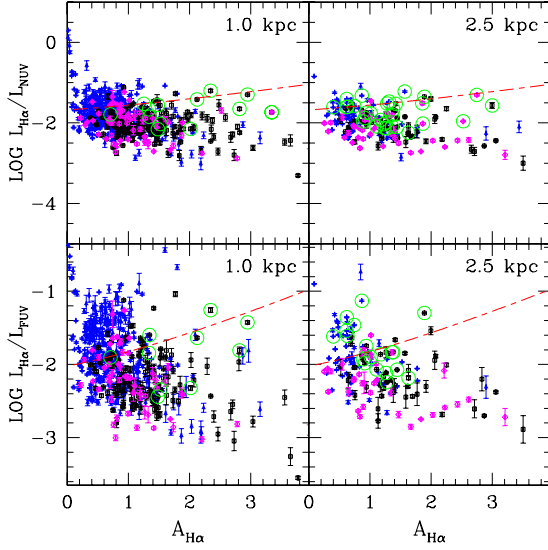


Fig. 14.— Plots of  $\log L_{H\alpha}/L_{NUV}$  vs.  $A_{H\alpha}$  (top panels) and  $\log L_{H\alpha}/L_{FUV}$  vs.  $A_{H\alpha}$  (bottom panels) for the 1.0 kpc radii aperture (left panels) and the 2.5 kpc radii aperture clumps (right panels). The open black squares are the disk clumps in the interacting galaxies, while the magenta open diamonds are the tidal clumps. The small blue filled triangles mark clumps in the disks of the spirals. The clumps circled in green have SFRs  $> 0.4 M_{\odot} \text{ yr}^{-1}$ . The red dashed lines show the expected relationship for the Calzetti dust attenuation law, combined with the NUV and FUV attenuations relative to the  $24 \mu\text{m}$  emission implied by the assumed SFR laws (see text).

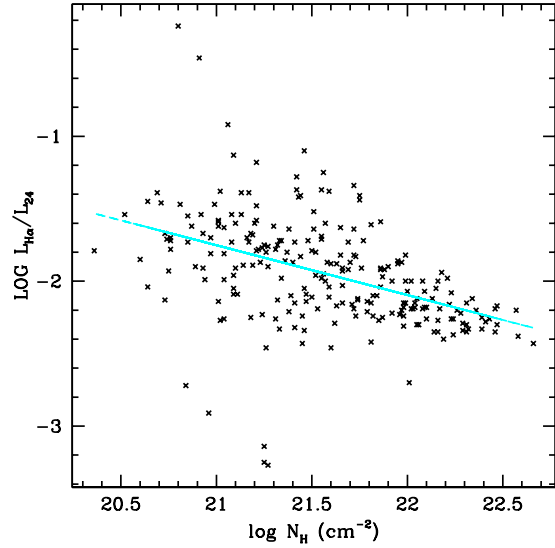


Fig. 15.— Plot of  $\log L_{H\alpha}/L_{24}$  vs.  $N_H$  within 500 pc regions in M51 using data from Kennicutt et al. (2007). Our best-fit straight line to the data is plotted in cyan.

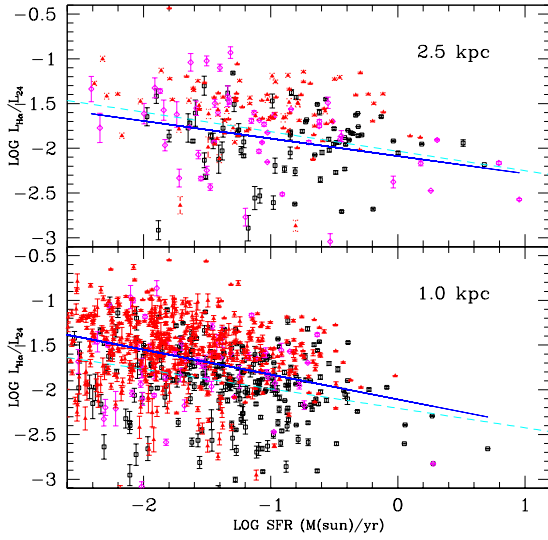


Fig. 16.— Plots of  $L_{H\alpha}/L_{24}$  vs. SFR for the 2.5 kpc clump sample (top panel) and the 1.0 kpc clump sample (bottom panel). The open black squares are the disk clumps in the interacting galaxies, while the magenta open diamonds are the tidal clumps. The small red filled triangles mark clumps in the disks of the spirals. The solid blue line displays the best linear fit to the data. The dashed cyan curve comes from the  $L_{H\alpha}/L_{24}$  vs.  $N_H$  relationship for M51 shown in Figure 15, along with the spatially-resolved Schmidt-Kennicutt law for M51 found by Kennicutt et al. (2007).

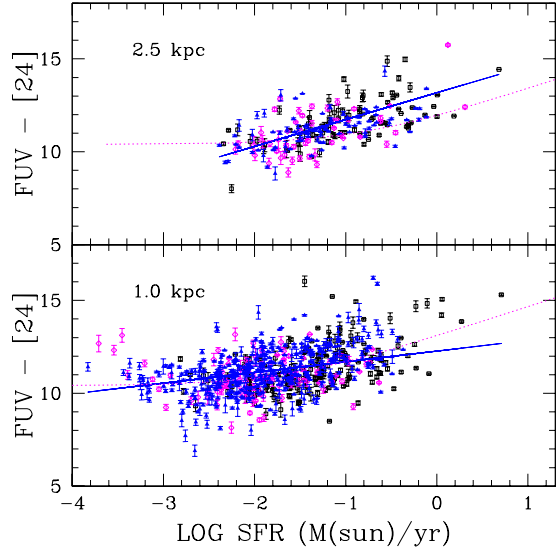


Fig. 17.— Plots of  $FUV - [24]$  vs. SFR for the 2.5 kpc clump sample (top panel) and the 1.0 kpc clump sample (bottom panel). The open black squares are the disk clumps in the interacting galaxies, while the magenta open diamonds are the tidal clumps. The small blue filled triangles mark clumps in the disks of the spirals. The solid blue line displays the best linear fit to the data. The dotted magenta curve gives the relation derived using the Boquien et al. (2013) M33  $\tau_{FUV}-N_H$  relation and the spatially-resolved Schmidt-Kennicutt law for M51 found by Kennicutt et al. (2007).

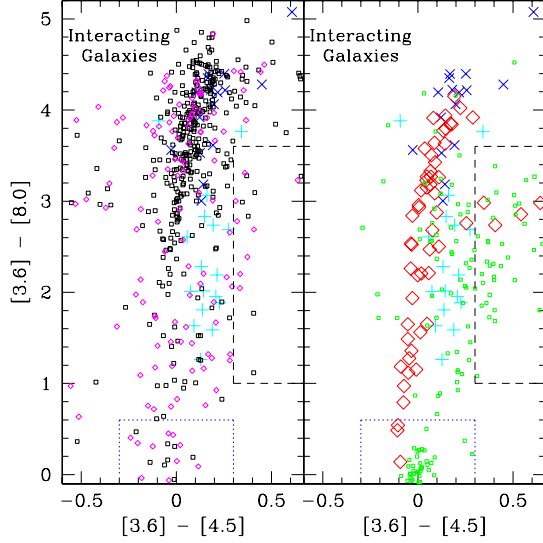


Fig. 18.— Left: For the 1.0 kpc sample of clumps, a plot of the Spitzer  $[3.6] - [4.5]$  vs.  $[3.6] - [8]$  colors for the clumps in the disks (small black squares) and in the tidal features (small magenta diamonds) of the interacting galaxies. Right: the same plot, but for the nuclei (red open diamonds) and ‘off’ galaxy sources (small green open squares). In both plots, the LMC (blue crosses) and SMC (cyan plus signs) regions from Lawton et al. (2010) are plotted. For clarity, errorbars are omitted in these plots. These are generally about the size of the data points or slightly larger. The blue dotted rectangle approximately marks the expected colors of foreground stars, while quasars are typically found in the black dashed rectangle. See the text for more details.

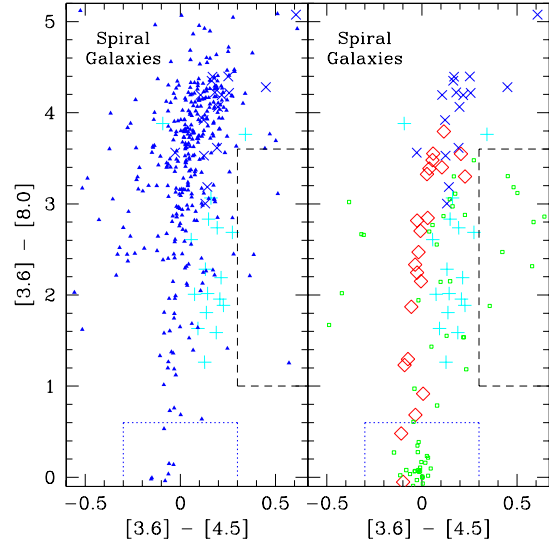


Fig. 19.— Similar to Figure 18, but for the 1.0 kpc aperture radii clumps in the spiral galaxies. The small blue filled triangles mark clumps in the disks of the spirals. Red open diamonds mark galactic nuclei, and ‘off’ galaxy sources are shown by small green open squares. In both plots, the LMC (blue crosses) and SMC (cyan plus signs) regions from Lawton et al. (2010) are plotted. Errorbars are omitted in these plots. These are generally about the size of the data points or slightly larger. The blue dotted rectangle approximately marks the expected colors of foreground stars, while quasars are typically found in the black dashed rectangle. See the text for more details.

TABLE 1  
INTERACTING GALAXY SAMPLE

| Arp<br>Name     | Other<br>Name(s)  | D <sup>†</sup><br>(Mpc) | log <sup>‡</sup><br>L <sub>FIR</sub><br>(L <sub>⊙</sub> ) | log<br>L <sub>Hα</sub><br>(erg s <sup>-1</sup> ) | Hα<br>Reference                |
|-----------------|-------------------|-------------------------|---|--|--------------------------------|
| Arp 24          | NGC 3445          | 33.1                    | 9.6   | 41.0   | This work: WHT                 |
| Arp 34          | NGC 4613/4/5      | 72.5                    | 10.2  | 41.6   | This work: WHT                 |
| Arp 65          | NGC 90/93         | 72.0                    | 9.5   | 40.8   | This work: WHT                 |
| Arp 72          | NGC 5994/6        | 53.4                    | 10.3  | 41.6   | This work: SARA                |
| Arp 82          | NGC 2535/6        | 59.2                    | 10.2  | 41.5   | Hancock et al. (2007)          |
| Arp 84          | NGC 5394/5        | 55.5                    | 10.8  | 41.4   | This work: WHT                 |
| Arp 85          | NGC 5194/5        | 12.1                    | 10.3  | 41.6   | Hoopes et al. (2001)           |
| Arp 86          | NGC 7752/3        | 65.9                    | 10.7  | ...  | ...                            |
| Arp 87          | NGC 3808          | 104.6                   | 10.9  | 41.6   | This work: WHT                 |
| Arp 89          | NGC 2648          | 31.8                    | 9.0   | 40.2   | This work: WHT                 |
| Arp 91          | NGC 5953/4        | 34.3                    | 10.4  | 41.4   | This work: WHT                 |
| Arp 102         | UGC 10814         | 104.7                   | 9.7   | 40.4   | This work: WHT                 |
| Arp 104         | NGC 5216/8        | 50.6                    | 10.5  | 41.2   | This work: WHT                 |
| Arp 105         | NGC 3561/UGC06224 | 126.2                   | 11.0  | 41.1   | This work: WHT                 |
| Arp 107         | UGC 5984          | 141.8                   | 10.1  | 41.6   | Smith et al. (2007)            |
| Arp 120         | NGC 4435/8        | 14.0                    | 9.2   | 40.1   | This work: WHT                 |
| Arp 178         | NGC 5613/4/5      | 82.5                    | 10.4  | 40.8   | This work: WHT                 |
| Arp 181         | NGC 3212/5        | 132                     | 10.6  | 40.8   | This work: WHT                 |
| Arp 188         | UGC 10214         | 134.2                   | 10.0  | 41.0   | This work: WHT                 |
| Arp 202         | NGC 2719          | 47.6                    | 9.8   | 41.4   | This work: SARA                |
| Arp 205         | NGC 3448/UGC6016  | 24.7                    | 9.8   | 40.9   | This work: WHT                 |
| Arp 240         | NGC 5257/8        | 101.7                   | 11.3  | 42.2   | Bushouse (1987)                |
| Arp 242         | NGC 4676          | 98.2                    | 10.7  | 41.4   | This work: WHT                 |
| Arp 244         | NGC 4038/9        | 24.1                    | 10.7  | 41.6   | This work: WHT                 |
| Arp 245         | NGC 2992/3        | 34.0                    | 10.4  | 40.8   | This work: WHT                 |
| Arp 253         | UGC 173/4         | 28.8                    | 8.7   | ...  | ...                            |
| Arp 256         |                   | 109.6                   | 11.1  | 42.0   | Bushouse (1987)                |
| Arp 261         |                   | 28.7                    | 9.3   | 40.8   | This work: WHT                 |
| Arp 269         | NGC 4485/4490     | 8.5                     | 9.8   | 40.2   | This work: WHT                 |
| Arp 270         | NGC 3395/6        | 29.0                    | 10.0  | 41.6   | Zaragoza-Cardiel et al. (2013) |
| Arp 271         | NGC 5426/7        | 40.0                    | 10.0  | 41.5   | This work: SARA                |
| Arp 279         | NGC 1253          | 22.6                    | 9.4   | 41.0   | This work: WHT                 |
| Arp 280         | NGC 3769          | 14.5                    | 9.1   | ...  | ...                            |
| Arp 282         | NGC 169           | 64.9                    | 10.1  | ...  | ...                            |
| Arp 283         | NGC 2798/9        | 29.6                    | 10.5  | 41.2   | SINGS                          |
| Arp 284         | NGC 7714/5        | 38.6                    | 10.1  | 41.8   | Smith et al. (1997)            |
| Arp 285         | NGC 2854/6        | 44.4                    | 10.1  | 41.2   | This work: WHT                 |
| Arp 290         | IC 195/6          | 46.5                    | 9.2   | 39.9   | This work: WHT                 |
| Arp 293         | NGC 6285/6        | 82.2                    | 11.1  | ...  | ...                            |
| Arp 294         | NGC 3786/8        | 43.6                    | ...   | 41.1   | This work: WHT                 |
| Arp 295         |                   | 94.2                    | 10.9  | ...  | ...                            |
| Arp 297N        | NGC 5753/5        | 139.3                   | 11.1  | 40.9   | This work: WHT                 |
| Arp 297S        | NGC 5752/4        | 70.2                    | 10.3  | ...  | ...                            |
| Arp 298         | NGC 7469/IC5283   | 66.4                    | 11.2  | ...  | ...                            |
| NGC 2207/IC2163 |                   | 38.0                    | 10.7  | 41.7   | Elmegreen et al. (2001)        |
| NGC 4567/8      |                   | 13.9                    | 9.9   | 40.9   | Koopmann et al. (2001)         |

<sup>†</sup>From the NASA Extragalactic Database (NED), using  $H_0 = 73$  km/s/Mpc, with Virgo, Great Attractor, and Shapley Supercluster infall models. <sup>‡</sup>Total 42.4 – 122.5  $\mu$ m far-infrared luminosity from the Infrared Astronomical Satellite (IRAS).

TABLE 2  
SPIRAL GALAXY SAMPLE

| Name<br>Name | Type   | D <sup>†</sup><br>(Mpc) | log <sup>‡</sup><br>L <sub>FIR</sub><br>(L <sub>⊙</sub> ) | log<br>L <sub>Hα</sub><br>(erg s <sup>-1</sup> ) | Hα<br>Reference                |
|--------------|--------|-------------------------|---|--|--------------------------------|
| NGC 24       | SAC    | 7.8                     | 8.2   | 40.0   | SINGS                          |
| NGC 337      | SBd    | 22.3                    | 9.9   | 41.2   | SINGS                          |
| NGC 628      | SAC    | 9.9                     | 9.6   | 41.3   | SINGS                          |
| NGC 925      | SABd   | 9.3                     | 9.1   | 40.7   | SINGS                          |
| NGC 1097     | SBb    | 16.5                    | 10.4  | 41.5   | SINGS                          |
| NGC 1291     | SBa    | 10.1                    | 8.6   | 40.9   | SINGS                          |
| NGC 2403     | SABcd  | 4.6                     | 9.2   | 41.2   | Van Zee et al. (in prep.)      |
| NGC 2543     | SBb    | 37.4                    | 9.9   | 41.2   | Epinat et al. (2008)           |
| NGC 2639     | SAa:?  | 49.6                    | 10.1  | 40.8   | This work: WHT                 |
| NGC 2841     | SAb    | 12.3                    | 9.2   | 40.8   | SINGS                          |
| NGC 2857     | SAC    | 71.0                    | 10.0  | ...  | ...                            |
| NGC 3049     | SBab   | 24.1                    | 9.4   | 40.9   | SINGS                          |
| NGC 3184     | SABcd  | 10.1                    | 9.3   | 41.0   | SINGS                          |
| NGC 3344     | SABbc  | 6.9                     | 9.0   | 40.6   | Dale et al. (2009)             |
| NGC 3353     | Sb?pec | 18.5                    | 9.5   | 40.8   | Hunter & Elmegreen (2004)      |
| NGC 3367     | SBc    | 47.6                    | 10.4  | 41.8   | Garcia-Barreto & Rosado (2001) |
| NGC 3521     | SABbc  | 8.0                     | 9.8   | 41.0   | SINGS                          |
| NGC 3621     | Sad    | 6.5                     | 9.4   | 41.2   | SINGS                          |
| NGC 3633     | SAa    | 41.0                    | 10.0  | ...  | ...                            |
| NGC 3646     | SAa    | 65.2                    | ...   | 41.8   | This work: WHT                 |
| NGC 3938     | SAC    | 15.5                    | 9.7   | 41.2   | SINGS                          |
| NGC 4254     | SAC    | 39.8                    | 11.1  | 42.5   | SINGS                          |
| NGC 4321     | SABbc  | 14.1                    | 10.0  | 41.0   | SINGS                          |
| NGC 4450     | SAab   | 14.1                    | 8.9   | 40.0   | SINGS                          |
| NGC 4559     | SABcd  | 9.8                     | 9.3   | ...  | ...                            |
| NGC 4579     | SABb   | 13.9                    | 9.4   | 40.9   | SINGS                          |
| NGC 4594     | SAa    | 12.7                    | 9.2   | ...  | ...                            |
| NGC 4725     | SABab  | 26.8                    | 10.0  | ...  | ...                            |
| NGC 4736     | SAab   | 4.8                     | 9.4   | 40.7   | Knapen et al. (2004)           |
| NGC 4826     | SAab   | 3.8                     | 9.0   | 40.1   | SINGS                          |
| NGC 5055     | SAbc   | 8.3                     | 9.8   | 41.1   | SINGS                          |
| NGC 5656     | Sab    | 51.4                    | 10.2  | ...  | ...                            |
| NGC 6373     | SABc   | 51.3                    | 9.2   | ...  | ...                            |
| NGC 6946     | SABcd  | 5.5                     | 9.9   | 41.0   | SINGS                          |
| NGC 7331     | SAb    | 14.4                    | 10.3  | 41.3   | SINGS                          |
| NGC 7793     | SAd    | 3.3                     | 8.6   | 39.9   | SINGS                          |
| UGC 4704     | Sdm:   | 10.4                    | ...   | ...  | ...                            |
| UGC 5853     | Scd:   | 132.6                   | 10.0  | ...  | ...                            |
| UGC 6879     | SABd?  | 37.3                    | 8.9   | ...  | ...                            |

<sup>†</sup>From the NASA Extragalactic Database (NED), using H<sub>0</sub> = 73 km/s/Mpc, with Virgo, Great Attractor, and Shapley Supercluster infall models. <sup>‡</sup>Total 42.4 – 122.5 μm far-infrared luminosity from the Infrared Astronomical Satellite (IRAS).